Multiplexed Volume Bragg Gratings in Narrow- and Broad-band Spectral Systems: Analysis and Application

A THESIS

SUBMITTED TO THE FACULTY OF THE GRADUATE SCHOOL

OF THE UNIVERSITY OF MINNESOTA

BY

Gregory B. Ingersoll

IN PARTIAL FULFILLMENT OF THE REQUIREMENTS

FOR THE DEGREE OF

DOCTOR OF PHILOSOPHY

James R. Leger

May, 2015

Acknowledgements

First and foremost, I would like to thank my advisor, Prof. Jim Leger. No doubt this process lasted much longer than either of us originally anticipated, but it led to a great deal of fruitful and interesting collaboration over the years.

Mike Scheidnes has long been a friend and collaborator at a few jobs and on countless engineering projects. His curiosity toward my work here led to many interesting discussions and several occasions to rethink the best way to describe things.

Next, I would like to thank Scott Nelson, a friend and colleague from my time working at Logic PD, for his interest in my work, my process, and my progress. Yes, I have been writing. Here is the result.

Finally, I would like to thank my family—in particular my mom and my brother—and friends Scott Hanson, Jon Larkowski, Anne Scheidnes, Matt Rengo, Matt Shursen, Scott Mehl, and many others. I strongly suspect that they were actually less interested in my research than they were in my sanity, and I cannot thank them enough.

Dedication

For my dad and grandpa, neither of whom got to see this but both of whom influenced my life in innumerable ways.

Abstract

Volume Bragg gratings (VBGs) are important holographic optical elements in many spectral systems. Using multiple volume gratings, whether multiplexed or arranged sequentially, provides advantages to many types of systems in overall efficiency, dispersion performance, flexibility of design, etc. However, the use of multiple gratings—particularly when the gratings are multiplexed in a single holographic optical element (HOE)—is subject to inter-grating coupling effects that ultimately limit system performance. Analyzing these coupling effects requires a more complex mathematical model than the straightforward analysis of a single volume grating. We present a matrix-based algorithm for determining diffraction efficiencies of significant coupled waves in these multiplexed grating holographic optical elements (HOEs). Several carefully constructed experiments with spectrally multiplexed gratings in dichromated gelatin verify our conclusions. Applications of this theory to broad- and narrow-band systems are explored in detailed simulations.

Broadband systems include spectrum splitters for diverse-bandgap photovoltaic (PV) cells. Volume Bragg gratings can serve as effective spectrum splitters, but the inherent dispersion of a VBG can be detrimental given a broad-spectrum input. The performance of a holographic spectrum splitter element can be improved by utilizing multiple volume gratings, each operating in a slightly different spectral band. However, care must be taken to avoid inter-grating coupling effects that

limit ultimate performance. We explore broadband multi-grating holographic optical elements (HOEs) in sandwiched arrangements where individual single-grating HOEs are placed in series, and in multiplexed arrangements where multiple gratings are recorded in a single HOE. Particle swarm optimization (PSO) is used to tailor these systems to the solar spectrum taking into account both efficiency and dispersion. Both multiplexed and sandwiched two-grating systems exhibit performance improvements over single-grating solutions, especially when reduced dispersion is required. Dispersion performance can be further improved by employing more than two VBGs in the spectrum splitter, but efficiency is compromised by additional cross-coupling effects.

Narrow-band applications of the multi-grating theory include spectral beam combining (SBC) systems. SBC systems utilizing multiple VBGs must be carefully analyzed to maximize channel density and efficiency, and thus output radiance. This analysis grows increasingly difficult as the number of channels in the system increases, and heuristic optimization techniques (e.g. PSO) are again useful tools for exploring the limits of these systems. We explore three classes of multi-grating SBC systems: "cascaded" where each grating adds a new channel to the system in sequence, "sandwiched" where several individual gratings are placed together and all channels enter the system at the same facet, and "multiplexed" where all of the gratings occupy the same holographic optical element (HOE). Loss mechanisms differ among these three basic classes, and the optimization algorithm shows that the highest channel density for a given minimum efficiency and fixed operating bandwidth is achieved for a cascaded-grating system. The multiplexed-grating system exhibits the lowest channel density under that same constraints but has the

distinct advantage of being realized by a single HOE. For a particular application, one must weigh channel density and efficiency versus system complexity when choosing among these basic classes of SBC system. Additionally, one may need to consider the effects of finite-width input beams. As input beam radius is reduced, angular clipping effects begin to dominate over spectral interference and crosstalk effects, limiting all three classes of SBC systems in a similar manner.

Contents

List of Tables

List of Figures

Chapter 1

Introduction

Volume Bragg gratings (VBGs) find uses in a wide range of spectral applications. Holographic optical elements (HOEs) employing these gratings provide high diffraction efficiency and narrow-band spectral characteristics to spectral beam combining (SBC) systems and wavelength division multiplexing (WDM) systems. Further, volume Bragg gratings can be designed with a broadband characteristic and applied to efficient power generation in spectrum splitting photovoltaic systems.

While single volume Bragg gratings are relatively simple to design and construct, there are limitations to the applicability of single grating HOEs in some applications. In beam combining, essentially only two channels (i.e. two sources operating at distinct center wavelengths) can be combined without resorting to a cascade of HOEs. Further, in a broad-spectrum application (e.g. solar spectrum splitting), the approximately sinc-squared nature of the grating's diffraction efficiency as a function of operating wavelength is a poor approximation to an

ideal spectral filter. For a single passband, a straightforward dichroic mirror may perform better. In addition, a volume grating, like any diffraction grating, is dispersive, and the dispersion over a wide band of interest can complicate the design of the system.

Combining multiple volume gratings in a single element adds design flexibility to these types of narrow- and broad-band systems. In a laser beam-combining system, multiplexed volume gratings allow multiple channels to be combined in a single HOE and also provide decoupling between the wavelength of a source and its physical position in the system. This decoupling is not generally available in spectral beam combining systems based on thin gratings, and dichroic filters lead to impractically complex arrangements in systems with many channels. In broadband applications, multiplexing gratings has two advantages: (1) the gratings can be tailored to better approximate an ideal spectral filter, and (2) the dispersive effects of the filter can be reduced by overlapping the output spectra of the multiplexed gratings.

Of course this design flexibility comes at the expense of complexity in the design and analysis of the HOE and often requires minimization of unwanted cross-coupling effects among multiplexed gratings. Efficient mathematical methods are needed to perform this analysis and to optimize systems that utilize multiplexed-grating HOEs. We present a novel method in Chapter 2 with experimental verification in Chapter 3.

Multiplexed volume Bragg gratings and mathematical methods for their analysis have indeed been previously studied for various applications. Many methods find their origins in Kogelnik's coupled-wave theory developed for single volume

gratings [1]. Subsequently, Alferness and Case studied cross-coupling (i.e. an input wave being coupled to multiple output waves) in two-grating monochromatic systems. Their mathematical methods were based on the so-called thin-grating decomposition [2, 3] or involved special cases of monochromatic two-grating systems for which analytical solutions of the coupled-wave equations could be found [4].

Other authors also offered solution methods for monochromatic two-grating systems including multiple-scattering theory [5], vector-synthetic gratings [6], and treatments of doubly-exposed gratings in both transmission [7] and reflection [8] modes. And Minier [9, 10] was one of the first to describe spectral interference effects in multiplexed grating systems operating at multiple wavelengths toward the development of narrowband WDM systems in planar waveguides. That work extended the coupled-wave equations to allow both angle and wavelength variation from the Bragg condition with the resulting equations solved through numerical integration. In addition, Moharam and Gaylord [11] presented their rigorous coupled-wave analysis which relies on a full solution to Maxwell's equations without approximations. This eliminates several assumptions present in Kogelnik's and in later work. Namely, the rigorous theory does not neglect boundary diffraction, does not eliminate second-derivatives stemming from the application of the wave equation (the "slowly-varying envelope approximation"), and does not assume a single diffracted wave from a grating.

The mathematical method for treating multiplexed-grating HOEs presented in Chapter 2 accepts the assumptions of Kogelnik's work to improve computational efficiency. This method is applied to the optimization of solar spectral splitting

systems in Chapter 4 and to spectral beam combining systems in Chapter 5. These types of broad- and narrow-band systems are discussed further in the following sections.

1.1 Solar Spectrum Splitters

Improving the efficiency of photovoltaic (PV) power generation systems is an important contemporary challenge. A key inefficiency in these systems is incomplete conversion of photon energy to electrical energy resulting from poor matching between semiconductor bandgap energies and photon energies across the incident spectrum. This inherent inefficiency in electrical conversion can be partially mitigated by employing multiple PV cells with bandgaps tailored to different parts of the solar spectrum. This is typically accomplished through the use of heterogenous bandgap semiconductors [12] or through optical spectrum splitting. The work presented here is related to the latter.

Rather than including multiple bandgaps on a single semiconductor substrate as heterogenous bandgap systems do, spectrum splitting systems [13–17] employ multiple separate PV cells with different bandgap energies. An optical system splits the incident spectrum such that spectral sub-bands impinge on semiconductors with bandgaps better tailored to them.

Spectrum splitting systems have the advantage of not being subject to the strict lattice-matching requirements of heterogeneous bandgap devices. However, spectrum splitting systems require additional low-loss optical elements to effect the splitting. One common architecture involves cascading dichroic filters to split the

incident spectrum and redirect sub-bands onto multiple diverse PV cells. Dichroic filters can have high reflection efficiency and sharp passband transitions, both of which are required for a high-performance spectrum splitter. However, transmission geometries are often preferred over reflection geometries. In addition, the performance of dichroic filters degrades for non-collimated light [18].

Filter performance for non-collimated light is important because PV cell systems often employ concentration (focusing) to improve efficiency. The short-circuit current in a PV cell increases linearly with illumination intensity. However, the open-circuit voltage is not constant—which would lead to constant efficiency with respect to illumination intensity—but rather increases logarithmically with illumination intensity [19]. This increase in output voltage at higher illumination intensity leads to higher power conversion efficiency within the PV cell.

In order to achieve concentration and indeed additional degrees of design flexibility in low- and non-concentrating systems, holographic optical elements (HOEs) are often employed as spectrum splitting components. HOEs can exploit the dispersive characteristics of planar volume gratings for basic spectrum splitting [20], include holographic lenses for concentration [21], and additionally include multiple gratings to improve performance over a range of incident angles [22].

For broadband applications such as solar spectrum splitting, employing multiple Bragg gratings also allows the engineer to tailor the spectral response of the system to better approximate an ideal filter. Additionally, the output spectra of the gratings can be overlapped in terms of angle thus reducing the impact of the dispersive effects of the holographic filter. These advantages of a multi-grating system can be realized whether separate HOEs are used for each grating and

subsequently sandwiched or the gratings are multiplexed into a single HOE. Optimization and performance analysis of sandwiched and multiplexed multi-grating spectrum splitters, specifically to improve filter efficiency and reduce dispersion effects, is detailed in Chapter 4.

1.2 Spectral Beam Combining

Spectral beam combining (SBC) systems are used to generate high laser radiance from several lower radiance sources. Unlike coherent beam combining (CBC) systems, the input sources for an SBC system all operate at different wavelengths, so the higher power at the output comes at the expense of a wider output bandwidth. However, SBC systems can be simpler to realize as they are not subject to constraints on the relative phases of the sources [23].

The literature proposes several architectures for SBC systems involving various fundamental optical components. The dispersion from a prism or from surface-relief diffraction gratings is often employed (in reverse) to combine several channels of different wavelengths [24–27]. Similar systems for wavelength division (de)multiplexing in communications systems were used as early as the 1970s [28, 29]. One drawback of these types of system is that they tightly couple the positions and wavelengths of the sources through the well-known grating equation. A representative diagram of a system of this type is shown in Fig. 1.1.

Coupling between source position and wavelength can be removed by utilizing volume holograms, where an individual volume Bragg grating (VBG) is used for each spectrally distinct source. Systems which only combine two beams often use

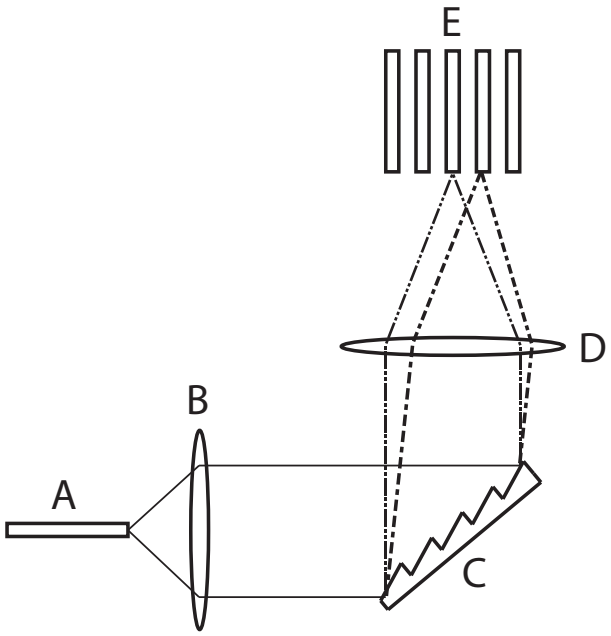

Figure 1.1: Representative spectral beam combiner—or WDM (de)multiplexer—using bulk optics and a blazed grating. (A) Output fiber, (B) focusing lens, (C) blazed reflection grating, (D) collimating lens, (E) source fibers. Dashed line styles indicate different wavelengths.

a single transmission-mode VBG which diffracts one of the beams while the other passes through undiffracted [30]. This type of system is shown in Fig. 1.2.

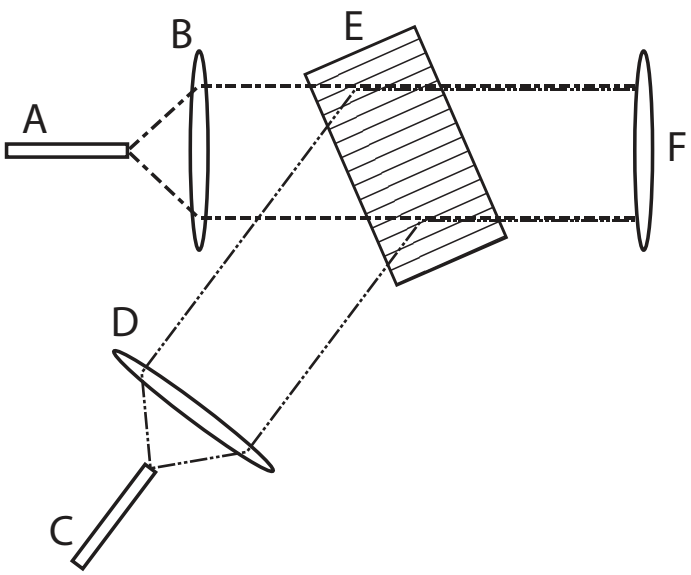

Figure 1.2: Representative spectral beam combining system utilizing a volume Bragg grating for combining two beams. The beam from source (A), collimated by lens (B), is not diffracted by the grating (E) and simply passes through the HOE. The beam from source (C), collimated by lens (D), is Bragg-matched with the grating and therefore is strongly diffracted into the common output direction. The two coaxial beams are then refocussed by lens (F).

Those systems combining more than two beams often utilize several individual reflection-mode VBGs which are organized sequentially such that another input source is added to an intermediate beam at each stage [31, 32]. Finally, there are SBC systems—and analogous wavelength division multiplexing (WDM) systems [33–35]—that employ a separate transmission-mode VBG for each input channel

but multiplex these gratings in a single holographic optical element (HOE). This last arrangement has obvious practical advantages because only a single optical element is required and alignment is simplified.

Regardless of whether the volume gratings in an SBC system are arranged sequentially or multiplexed into a single HOE, the system is subject to inter-grating interference and cross-coupling effects that limit overall efficiency and introduce stray light into the system. Previous related work from the literature for WDM systems often simply suggests increasing the channel spacing to 1.5 [36] or three times [37] or more the individual channel width so that the gratings operate essentially independently. This simplifies the analysis in many ways but also could unnecessarily increase the overall bandwidth of the system depending on competing requirements.

If a narrow operating bandwidth is a goal as well as high-efficiency, more sophisticated techniques must be used to optimize such systems. In particular, an optimization algorithm can position sources in space (i.e. set their angles of incidence) and spectrum (i.e. set the center wavelengths of the channels) and also prescribe the material thickness–which has a strong effect on channel width–in order to maximize channel density and overall combining efficiency.

In Chapter 4, we present optimization and performance analysis of three classes of multi-grating spectral beam combining system: cascaded-grating, sandwiched-grating, and multiplexed-grating. We consider relative performance for both plane-wave and finite-beam inputs.

1.3 Research Objectives

The following chapters of this document expand on the ideas introduced thus far by:

1. Developing a matrix-based algorithm for calculating diffraction efficiency in holographic optical elements comprised of multiplexed volume Bragg gratings. Deviations from the Bragg condition in both wavelength and angle can be treated by the algorithm simultaneously. Transmission- and reflection-mode phase gratings can also be treated simultaneously. Detailed spectral experiments verify the algorithm.

2. Exploring performance improvements to volume holographic spectrum splitters based on sequential- and multiplexed-grating HOEs. System optimization shows that dispersion performance is improved through employment of additional gratings in a two-band spectrum splitter.

3. Identifying relative limitations of sequential- and multiplexed-grating spectral beam combining systems in the presence of inter-grating interference for both plane-wave and finite-beam inputs.

The research in this dissertation has resulted in the following journal publications and conference proceedings:

1. G. B. Ingersoll and J. R. Leger, "Spectral interference in multiplexed volume Bragg gratings: theoretical calculations and experimental verification," Applied Optics **53**, 5477 (2014).

2. G. B. Ingersoll and J. R. Leger, Department of Electrical and Computer Engineering, University of Minnesota, 200 Union St. SE, Minneapolis, MN, 55455, USA, are preparing a manuscript to be called "Channel density and efficiency optimization of volume Bragg grating based spectral beam combining systems in sequential and multiplexed arrangements."

3. G. B. Ingersoll and J. R. Leger, Department of Electrical and Computer Engineering, University of Minnesota, 200 Union St. SE, Minneapolis, MN, 55455, USA, are preparing a manuscript to be called "Optimization of multi-grating volume holographic spectrum splitters for photovoltaic applications."

4. G. B. Ingersoll and J. R. Leger, "Theoretical analysis of multiplexed volume holograms for spectral beam combining," Proc. SPIE **7195**, 71951P (2009).

5. G. B. Ingersoll, D. Lin, and J. R. Leger, "Experimental verification of spectral grating interference in multiplexed volume holograms employed as broadband dispersive elements for solar concentrators," Proc. SPIE **8821**, 882107 (2013).

Chapter 2

Matrix Method for Modeling Multiplexed Volume Gratings

In this chapter, we conduct an in-depth study of spectral interference in multiplexed volume holograms and derive a new mathematical method for calculating the diffraction efficiency of these multiplexed grating systems. The mathematical method presented here starts by constructing a characteristic matrix for the grating system, and includes an algorithm to select a set of significant plane-wave diffraction orders to preserve for the analysis. The diffraction efficiencies of the various waves are then computed through straightforward eigenvector decomposition of the matrix. This method is quite flexible for holograms consisting of many gratings, and allows for calculations of direct- and cross-coupled orders as a function of both incident angle and operating wavelength. The method is also fast as it relies on efficient matrix-manipulation techniques rather than numerical

integration. The overall theory of spectral interference presented in this chapter is verified experimentally for a broad-spectrum multiplexed grating pair in Chapter 3.

The mathematical model for quickly calculating diffraction efficiencies in systems of multiplexed volume gratings begins with the well-known model described by Kogelnik [1]. Section 2.1 begins with a summary of Kogelnik's symbology and the differential equations describing coupled waves in a single planar volume transmission phase grating. We then convert this model to a matrix formulation before expanding the matrix solution in Section 2.2 to treat arbitrary systems of multiplexed plane gratings with plane wave inputs at arbitrary incident angles and wavelengths. In Appendix B, the model is extended further to include volume reflection gratings in addition to transmission-mode gratings.

2.1 Single Transmission Mode Grating

A single planar volume grating is typically depicted conceptually in a momentum or k-space diagram as in Fig. 2.1. Here, the radius of the circle is $\beta = 2\pi n/\lambda$ where n is the bulk index of refraction of the material. Two plane waves are present in the system and are referred to as the reference and signal waves with field symbols R and S and vector symbols $\boldsymbol{\rho}$ and $\boldsymbol{\sigma}$ respectively. The figure can be interpreted as the condition for grating construction where $\boldsymbol{\rho}$ and $\boldsymbol{\sigma}$ are given and the grating vector, $\boldsymbol{K}$, is equal to $\boldsymbol{\rho} - \boldsymbol{\sigma}$. The figure can also be interpreted as the situation for grating reconstruction where $\boldsymbol{\rho}$ and $\boldsymbol{K}$ are given and $\boldsymbol{\sigma}$ is derived. This second interpretation leads to the differential equations used to calculate

diffraction efficiency for a given input wave.

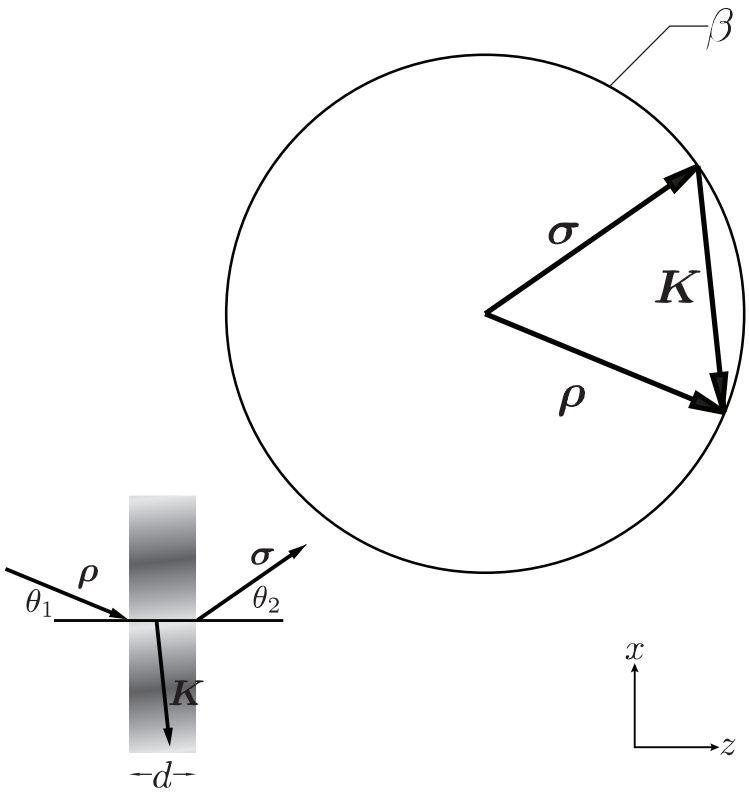

Figure 2.1: Momentum or k-space diagram for a single grating. Inset: the physical model of a single grating defining plane wave angles, θ_1 and θ_2, and the grating thickness, d.

The inset in Fig. 2.1 shows a physical representation of a volume grating in a simplified two-dimensional system. This grating can be created in a suitable holographic material of thickness d by interfering two coherent plane waves of wavelength λ traveling at angles θ_1 and θ_2 with respect to the optical axis (here z) [38, Section 9.7.1]. During construction, it is assumed that the holographic material responds linearly to exposure intensity resulting in a sinusoidal variation

of the index of refraction of the bulk material given by:

$$\epsilon(x, y, z) = \epsilon_0 + \epsilon_1 \cos\left((\boldsymbol{\rho} - \boldsymbol{\sigma}) \cdot \boldsymbol{x}\right) = \epsilon_0 + \epsilon_1 \cos\left(\boldsymbol{K} \cdot \boldsymbol{x}\right) \tag{2.1}$$

where $\epsilon_0 = n^2$.

During reconstruction, the electric field in the material is assumed to be the sum of two plane waves each polarized perpendicular to the plane of incidence:

$$E(x, y, z, t) = R(z)e^{j(\boldsymbol{\rho}\cdot\boldsymbol{x} - \omega t)} + S(z)e^{j(\boldsymbol{\sigma}\cdot\boldsymbol{x} - \omega t)}. \tag{2.2}$$

in which the amplitudes of the two waves are assumed to be functions of z only. Combining Eq. 2.1 and Eq. 2.2 with the familiar scalar wave equation and dropping second derivatives in z—Kogelnik's assumption that "energy interchange between S and R is slow"—leads to the system of first-order differential equations:

$$c_R R' = j\kappa S \tag{2.3a}$$

$$c_S S' - j\vartheta S = j\kappa R \tag{2.3b}$$

Here primes indicate first derivatives in z, and $\kappa = \pi n_1/\lambda$ where n_1 is the index modulation of the grating given by:

$$n_1 = \frac{\epsilon_1}{2\sqrt{\epsilon_0}}. \tag{2.4}$$

Also, c_R and c_S are the respective direction cosines of the two significant waves:

$$c_R = \cos\theta_1 = \frac{\rho_z}{\beta} \tag{2.5a}$$

$$c_S = \cos\theta_1 - \frac{|\boldsymbol{K}|}{\beta}\cos\phi = \frac{\sigma_z}{\beta} \tag{2.5b}$$

where ϕ is the tilt of the grating relative to the z-axis. Finally, ϑ is the dephasing parameter defined as:

$$\vartheta = \frac{\beta^2 - \sigma^2}{2\beta} = |\boldsymbol{K}|\cos(\phi - \theta) - \frac{|\boldsymbol{K}|^2}{4\pi n}\lambda \tag{2.6}$$

By assuming solutions of the form $R(z) = ae^{\gamma z}$ with a constant, the system of differential equations can be written in matrix form as

$$\boldsymbol{M}\boldsymbol{x} = \gamma\boldsymbol{x} \tag{2.7}$$

where

$$\boldsymbol{M} = \begin{bmatrix} 0 & \frac{j\kappa}{c_R} \\ \frac{j\kappa}{c_S} & \frac{j\vartheta}{c_S} \end{bmatrix} \tag{2.8a}$$

$$\boldsymbol{x} = \begin{bmatrix} R \\ S \end{bmatrix} \tag{2.8b}$$

For the eigenvectors of $\boldsymbol{M}$ to form an orthonormal basis, $\boldsymbol{M}$ must be symmetric [39]. We can achieve this criterion without loss of generality through a simple

variable substitution where we define

$$\tilde{\boldsymbol{x}} \equiv \begin{bmatrix} \tilde{R} \\ \tilde{S} \end{bmatrix} \equiv \begin{bmatrix} c_R & 0 \\ 0 & \sqrt{c_R c_S} \end{bmatrix} \boldsymbol{x}. \tag{2.9}$$

Use of variable substitution results in the symmetric matrix

$$\tilde{\boldsymbol{M}} = \begin{bmatrix} 0 & \frac{j\kappa}{\sqrt{c_R c_S}} \\ \frac{j\kappa}{\sqrt{c_R c_S}} & \frac{j\vartheta}{c_S} \end{bmatrix}. \tag{2.10}$$

The eigenvalues of $\tilde{\boldsymbol{M}}$ are found in the usual fashion by solving

$$\begin{vmatrix} \gamma & \frac{-j\kappa}{\sqrt{c_R c_S}} \\ \frac{-j\kappa}{\sqrt{c_R c_S}} & \gamma - \frac{j\vartheta}{c_S} \end{vmatrix} = 0 \tag{2.11}$$

which gives

$$\gamma_{\pm} = \frac{j}{2}\left(\frac{\vartheta}{c_S} \pm \sqrt{\frac{\vartheta^2}{c_S^2} + \frac{4\kappa^2}{c_R c_S}}\right) \tag{2.12}$$

Defining $\boldsymbol{\xi}_+$ and $\boldsymbol{\xi}_-$ as the (column) eigenvectors of $\tilde{\boldsymbol{M}}$ corresponding to γ_+ and γ_- respectively, we can use the eigenvalues and the matrices representing the variable substitution to define the transfer matrix of a grating of thickness d as:

$$\boldsymbol{G} = \begin{bmatrix} \frac{1}{c_R} & 0 \\ 0 & \frac{1}{\sqrt{c_R c_S}} \end{bmatrix} \begin{bmatrix} \boldsymbol{\xi}_+ & \boldsymbol{\xi}_- \end{bmatrix} \begin{bmatrix} e^{\gamma_+ d} & 0 \\ 0 & e^{\gamma_- d} \end{bmatrix} \begin{bmatrix} \boldsymbol{\xi}_+ & \boldsymbol{\xi}_- \end{bmatrix}^T \begin{bmatrix} c_R & 0 \\ 0 & \sqrt{c_R c_S} \end{bmatrix} \tag{2.13}$$

such that the amplitudes of the R and S waves at the input ($z = 0$) and output

$(z = d)$ of the grating are related by:

$$\boldsymbol{x}_d = \boldsymbol{G}\boldsymbol{x}_0. \tag{2.14}$$

The boundary conditions for a transmission grating are such that the amplitude of the R wave at $z = 0$ is 1 and the amplitude of the S wave at $z = 0$ is 0. Given these values for the components of $\boldsymbol{x}_0$, the diffraction efficiency of the grating is given by

$$\eta = \frac{c_S}{c_R} S_d S_d^* \tag{2.15}$$

where S_d is the S-element of $\boldsymbol{x}_d$. This matches Kogelnik's result for a transmission phase grating.

2.2 Multiplexed Gratings

Converting Kogelnik's single grating method to an explicit matrix solution has multiple benefits. This technique can provide insight into the energy exchange between significant waves that may not be clear from the basic differential equations (Eq. 2.3). This is explored further in Appendix A. However, the value of the matrix solution becomes especially clear when one must deal with multiple simultaneous gratings under variations in the incident angle and wavelength of the reference wave. Formulating the solution in this way allows a rather straightforward algorithm to determine the N significant waves present in the compound hologram and to build the $N \times N$ characteristic matrix, $\tilde{\boldsymbol{M}}$.

A typical situation involving two multiplexed gratings is shown in Fig. 2.2.

Here, the gratings ($\boldsymbol{K}_1$ and $\boldsymbol{K}_2$) share one of their defining angles—note the common direction of $\boldsymbol{\rho}_1$ and $\boldsymbol{\rho}_2$—and have different defining wavelengths denoted by β_1 and β_2. This system could define, for example, a spectrum splitter (Chapter 4) or a spectral beam combiner (Chapter 5).

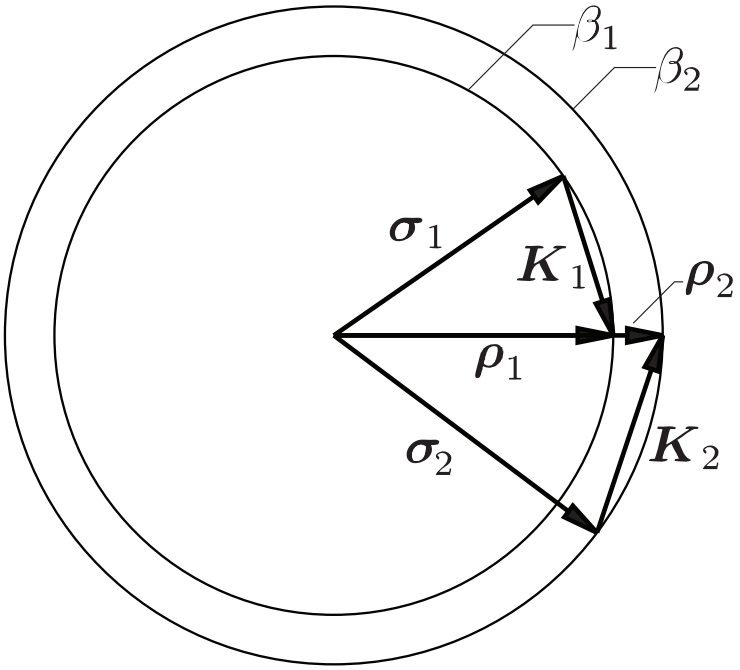

Figure 2.2: k-space diagram for defining two multiplexed gratings. These gratings share one of their defining angles and have different central operating wavelengths.

When this pair of gratings is reconstructed by a plane wave, $\boldsymbol{\rho} = \boldsymbol{\rho_1}$, the momentum diagram appears as in Fig. 2.3. Here, there are two directly coupled waves, $\boldsymbol{\sigma}_1 = \boldsymbol{\rho} - \boldsymbol{K}_1$ and $\boldsymbol{\sigma}_2 = \boldsymbol{\rho} - \boldsymbol{K}_2$. The input wave is Bragg-matched with $\boldsymbol{K}_1$—the corresponding output vector terminates on the momentum circle—and the input wave is nearly Bragg-matched with $\boldsymbol{K}_2$. Note that because this situation involves different defining wavelengths for the multiplexed gratings, an input wave cannot, in general, be Bragg-matched with all of the gratings simultaneously.

This condition precludes the analytical solution shown by Case for a two-grating monochromatic system [4]. (In Case's work, a single wavelength was used and again the two gratings shared one common angle. A plane wave with the given wavelength and incident at the gratings' common angle would be Bragg-matched with both gratings resulting in all of the dephasing parameters analogous to ϑ going to zero. This simplification to the differential equations describing the system allows an analytical solution for this special case.)

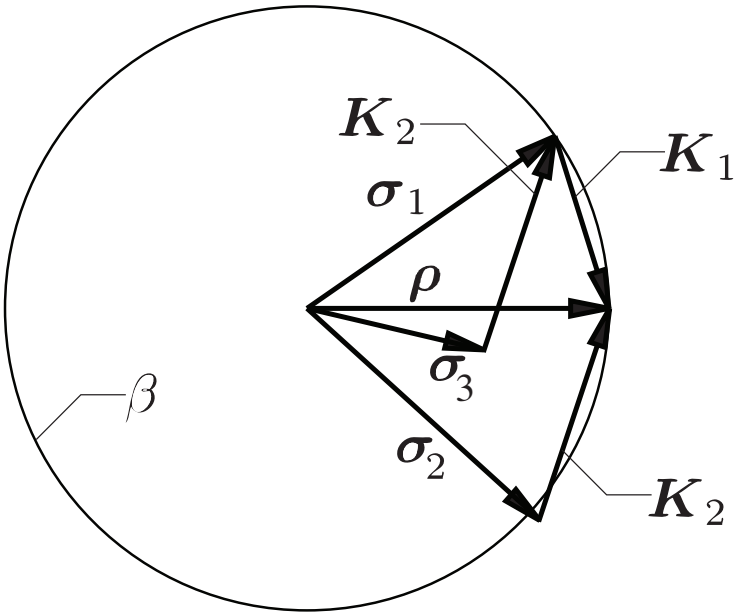

Figure 2.3: k-space diagram for reconstructing two multiplexed gratings. From the diagram, waves associated with $\boldsymbol{\sigma}_1$ and $\boldsymbol{\sigma}_2$ are qualitatively expected to be significant to the solution. However, $\boldsymbol{\sigma}_3$ is not qualitatively expected to be significant because $|\boldsymbol{\sigma}_3|$ differs so greatly from β.

In addition to the two directly coupled waves, Fig. 2.3 also depicts a wave that derives from interaction with both gratings ($\boldsymbol{\sigma}_3 = \boldsymbol{\sigma}_1 - \boldsymbol{K}_2 = \boldsymbol{\rho} - \boldsymbol{K}_1 - \boldsymbol{K}_2$). This cross-coupled wave must be included in the mathematical model in order to

achieve accurate results. (This concept was detailed for monochromatic systems in [3]).

The algorithm for building the characteristic matrix for a multiplexed system then proceeds as follows. Given the input wavevector and the grating vectors, all combinations of directly-coupled waves ($\boldsymbol{\sigma}_j = \boldsymbol{\rho} \pm \boldsymbol{K}_i$) are constructed. Some of these vector combinations will turn out to be insignificant to the diffraction efficiency calculation especially when their wave vectors terminate far from the momentum circle. (This can be seen qualitatively for $\boldsymbol{\sigma}_3$ in Fig. 2.3). This is equivalent to a wave having a large dephasing parameter (see Eq. 2.6), so the dephasing parameter is used in the algorithm as a measure for eliminating waves from consideration.

Those waves with dephasing parameters exceeding some limit are eliminated, and then cross-coupled waves are determined through vector combination of the directly-coupled wavevectors and the grating vectors. Again, insignificant waves are eliminated. This process continues through a pre-determined number of diffraction stages or until a diffraction stage results in no new significant waves.

An appropriate limit for the dephasing parameter is dependent on the exact nature of the system being modeled and must be determined iteratively. If the limit is set too low, waves with significant energy could be eliminated from the model leading to inaccurate results and poor system optimization. Conversely, if the limit is set too high, the size of the characteristic matrix of the system increases unnecessarily, leading to longer execution times for the calculations with no significant difference in the end result.

One technique for determining the dephasing limit for a given system is to set

a relatively high limit and then calculate diffraction efficiencies of the significant waves for a sparse collection of input wavelengths. If the diffraction efficiency of any included waves in the domain of interest does not exceed some small value (e.g. 0.1%), the dephasing limit can be reduced to eliminate these waves from the model. Then the diffraction efficiencies of the significant waves can be more quickly calculated for a dense set of inputs.

When all significant waves are determined, the characteristic matrix, $\tilde{\boldsymbol{M}}$, for the system can be constructed directly. Diagonal elements consist of functions of the respective waves' dephasing parameters. ϑ corresponding to the reference wave, $\boldsymbol{\rho}$, is by definition zero, so $\tilde{\boldsymbol{M}}_{00} = 0$. Other diagonal elements follow:

$$\tilde{\boldsymbol{M}}_{mm} = \frac{j\vartheta_m}{c_{Sm}}, \quad m \neq 0 \tag{2.16}$$

Conceptually, off-diagonal elements link waves to each other through gratings. These elements are functions of the two waves' direction cosines and of the grating's coupling coefficient, κ. If wave m and wave n are coupled through grating p, the corresponding (symmetric) matrix elements become:

$$\tilde{\boldsymbol{M}}_{mn} = \tilde{\boldsymbol{M}}_{nm} = \frac{j\kappa_p}{\sqrt{c_{Sm}c_{Sn}}}, \quad m \neq n \tag{2.17}$$

For example, referencing Fig. 2.3, grating 2 couples wave S_1 (corresponding to $\boldsymbol{\sigma}_1$) to wave S_3, so the corresponding matrix elements are:

$$\tilde{\boldsymbol{M}}_{13} = \tilde{\boldsymbol{M}}_{31} = \frac{j\kappa_2}{\sqrt{c_{S1}c_{S3}}} \tag{2.18}$$

Likewise, grating 1 couples the reference wave to wave S_1 leading to off-diagonal elements:

$$\tilde{\boldsymbol{M}}_{01} = \tilde{\boldsymbol{M}}_{10} = \frac{j\kappa_1}{\sqrt{c_R c_{S1}}} \tag{2.19}$$

All other matrix elements are 0, so for the system depicted in Fig. 2.3, assuming ϑ_3 is quantitatively small enough such that wave S_3 is not eliminated, the non-zero elements in the 4×4 characteristic matrix follow:

$$\tilde{\boldsymbol{M}} = \begin{bmatrix} 0 & \cdot & \cdot & 0 \\ \cdot & 0 & 0 & \cdot \\ \cdot & 0 & \cdot & 0 \\ 0 & \cdot & 0 & \cdot \end{bmatrix} \tag{2.20}$$

(Recall that the reference wave is Bragg-matched with grating 1, so $\vartheta_1 = 0$ and $\tilde{\boldsymbol{M}}_{11} = 0$.)

So far TE-polarization (i.e. electric field vectors perpendicular to the plane of incidence) has been assumed. However, TM-polarization, or indeed arbitrary polarization, can be handled in the model at this point with a straightforward addition to the characteristic matrix. This becomes especially important when we discuss solar splitting applications in Chapter 4.

Again, following [1], the coupling between two waves S_m and S_n is reduced by the dot product of their respective (normalized) polarization vectors, $\langle \boldsymbol{s}_m \cdot \boldsymbol{s}_n \rangle$, resulting in a more general form for Eq. 2.17:

$$\tilde{\boldsymbol{M}}_{mn} = \tilde{\boldsymbol{M}}_{nm} = \frac{j\kappa_p \langle \boldsymbol{s}_m \cdot \boldsymbol{s}_n \rangle}{\sqrt{c_{Sm} c_{Sn}}}, \quad m \neq n \tag{2.21}$$

Once the characteristic matrix has been fully determined, the relative power distribution among all of the significant waves is calculated in a method analogous to the discussion above. Continuing with the example system of Fig. 2.3, the transfer matrix, Eq. 2.22, is built in an analogous fashion to Eq. 2.13.

$$\boldsymbol{G} = \begin{bmatrix} \frac{1}{c_R} & 0 & 0 & 0 \\ 0 & \frac{1}{\sqrt{c_R c_{S1}}} & 0 & 0 \\ 0 & 0 & \frac{1}{\sqrt{c_R c_{S2}}} & 0 \\ 0 & 0 & 0 & \frac{1}{\sqrt{c_R c_{S3}}} \end{bmatrix} \begin{bmatrix} \boldsymbol{\xi}_1 & \boldsymbol{\xi}_2 & \boldsymbol{\xi}_3 & \boldsymbol{\xi}_4 \end{bmatrix} \begin{bmatrix} e^{\gamma_1 d} & 0 & 0 & 0 \\ 0 & e^{\gamma_2 d} & 0 & 0 \\ 0 & 0 & e^{\gamma_3 d} & 0 \\ 0 & 0 & 0 & e^{\gamma_4 d} \end{bmatrix} \times \begin{bmatrix} \boldsymbol{\xi}_1 & \boldsymbol{\xi}_2 & \boldsymbol{\xi}_3 & \boldsymbol{\xi}_4 \end{bmatrix}^T \begin{bmatrix} c_R & 0 & 0 & 0 \\ 0 & \sqrt{c_R c_{S1}} & 0 & 0 \\ 0 & 0 & \sqrt{c_R c_{S2}} & 0 \\ 0 & 0 & 0 & \sqrt{c_R c_{S3}} \end{bmatrix} \tag{2.22}$$

and the individual field amplitudes are found analogously to Eq. 2.14:

$$\boldsymbol{x}_d = \begin{bmatrix} R_d \\ S_{1d} \\ S_{2d} \\ S_{3d} \end{bmatrix} = \boldsymbol{G} \begin{bmatrix} 1 \\ 0 \\ 0 \\ 0 \end{bmatrix} \tag{2.23}$$

Finally, the diffraction efficiencies of the individual waves are found from:

$$\eta_i = \frac{c_{Si}}{c_R} S_{id} S_{id}^* \tag{2.24}$$

Using optimized libraries of standard matrix operations (e.g. architecture-specific implementations of BLAS, LAPACK, ATLAS, etc.), these calculations execute quickly even for 10×10 and larger matrices. While rigorous coupled-wave methods are not used, the approximations employed here allow for this efficient calculation method which, in turn, provides for efficient optimization algorithms for systems of multiplexed volume gratings.

To ensure that these approximations do not preclude accurate results, we verified this mathematical model through the spectral experiments detailed in the next chapter. This model is applicable to both broad- and narrow-band spectral systems where maximizing efficiency is a design goal, and these two subclasses are explored in subsequent chapters. Holographic spectrum splitters, explored in Chapter 4, are fitting broadband systems. Narrow-band spectral beam combining systems are explored in Chapter 5. Because the focus in these application chapters is on transmission gratings, a discussion of how to extend this method to support volume reflection gratings is relegated to Appendix B.

Chapter 3

Experimental Verification of the Matrix Method

To demonstrate the validity of the mathematical model developed in Chapter 2, we constructed multiplexed gratings in PFG–04 dichromated gelatin. The efficiency of various diffraction orders were then characterized as a function of input wavelength and compared to the model.

3.1 Grating Design and Construction

The experimental setup for multi-grating hologram construction is depicted in Fig. 3.1. The exposure source used for the experiment was a Coherent Verdi laser operating at 532nm and 5 watts. The beam from this source was split, filtered, expanded, and collimated. Then each individual beam was redirected to the holographic plate by mirrors mounted on rotation stages. The mirrors were

rotated to set each beam's angle relative to the plate. These angles and the laser wavelength completely determine the period and tilt of the resulting gratings.

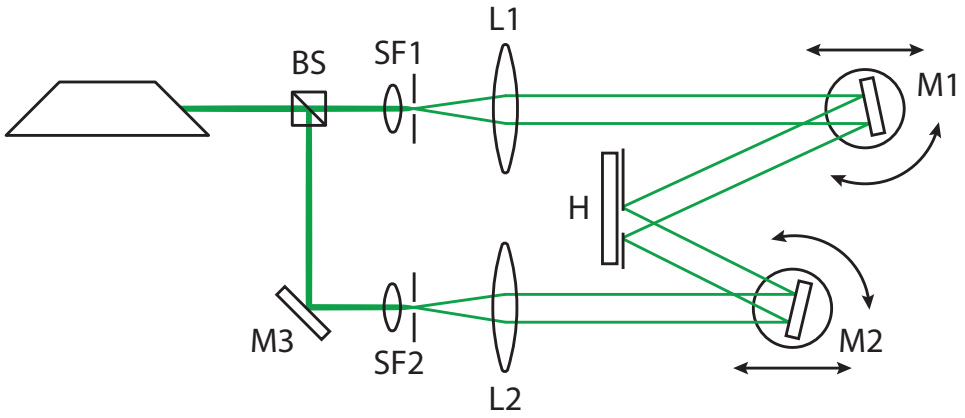

Figure 3.1: Experimental setup for hologram construction. The laser source is sent through a beam splitter (BS), and each arm passes through a spatial filter (SF1 and SF2). Each arm is then collimated by lenses L1 and L2. Mirrors M1 and M2 are allowed to rotate and translate thus redirecting each beam arm onto the holographic plate (H) at a particular position and incident angle. A mask is placed directly on the surface of the plate to limit the exposed area.

The steering mirrors in the exposure setup were also allowed to translate along one axis in order to set the position of the overlap of the two beams on the plate. (Note that the coherence length of this laser is greater than 20m, so path-length matching of the beams on the scale of the optical tabletop is of little concern.) Translating the mirrors allowed for multiple experiments on a single plate, and, more importantly, allowed the two exposures of a particular experiment to only partially overlap. This in turn allowed characterization of each grating individually as well as characterization of the multiplexed pair as we discuss in Section 3.3.

We used the mathematical model to determine period and tilt parameters for a

grating pair that would operate over much of the visible spectrum. This pair was also designed to exhibit easily measurable cross-coupling over a sufficiently wide wavelength range. Exposure energies—beam intensity, beam balance ratio, and exposure time—were determined iteratively to achieve the desired peak diffraction efficiency which was deliberately kept low in these experiments to avoid saturating the holographic material.

Data from the literature [40] suggests that the effective dynamic range of PFG–04 dichromated gelatin plates corresponds to an index modulation, n_1, of approximately 0.012. In order to avoid clipping the desired sinusoidal index variation through multiple exposures, a relatively low exposure energy was used for these experiments. Staying well within the dynamic range of the material ensured that any diffraction orders evident during hologram reconstruction were a result of grating direct- and cross-coupling predicted by the mathematical model and not the result of non-linear effects of the material.

3.2 HOE Development and Processing

Our experimental holographic material was commercially-available 60mm square glass plates with a coating of PFG–04 dichromated gelatin on one side. After completing the exposures for a set of plates, the plates must be developed prior to measurement and characterization of the gratings. Because the sensitivity peak of the undeveloped PFG–04 material is approximately 514nm, all exposures must be made and all subsequent processing must be performed under "safe", red light.

The first step in processing the plates is to bake them at approximately 100°C

for 20 minutes to partially dehydrate and harden the surface layer of the gelatin. (The duration of this baking step is dependent on the age of the plates.)

While the plates are baking, we prepare four pans for soaking the plates. The first pan simply contains cold water. Using water that is too warm can result in cloudiness in the finished plate, but cold tap water provided good results. The next pan contains a 50:50 (by volume) solution of isopropanol and cold water. The third pan contains a 75:25 (by volume) solution of isopropanol and cold water. The final pan contains 100% isopropanol.

Following the initial baking period, the plates are placed in cold water for three minutes. After this, the plates are moved to the 50:50 water and alcohol solution for three minutes, and so on. After the final bath, we remove surface liquid from the plates with compressed air and then return the plates to the oven (again set to approximately 100°C) for 60 minutes.

Even after developing in this manner, the recorded holograms can degrade over time. This is especially a concern in humid conditions because the degradation is primarily due to the gelatin absorbing atmospheric moisture. We sealed the holographic plates used for the experiments in this chapter with a second clear glass plate and a layer of UV-cure optical adhesive.

3.3 Measurement

In order to reduce the impact of material and exposure inconsistency given our operating regime, the multiplexed gratings were exposed on the holographic plate with only partial overlap as depicted in Fig. 3.2. This allowed each grating to be

characterized individually. The single gratings' diffraction orders were measured as a function of input angle using a 632nm laser source as depicted in Fig. 3.3. Angle was used as the free variable because the grating period and tilt can be largely determined by finding the two input angles at which there is a diffraction efficiency peak for a fixed wavelength. This cannot be achieved through a variation in wavelength alone.

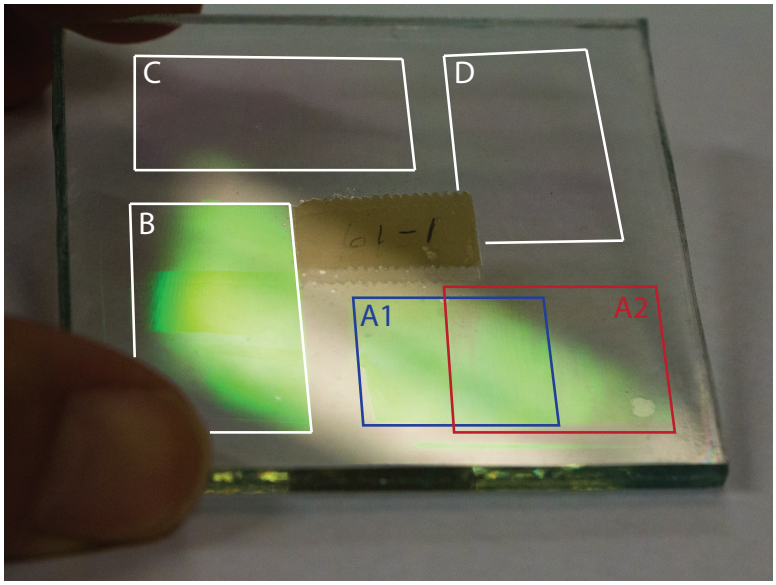

Figure 3.2: Layout of experimental gratings on a holographic plate. Four sets of two gratings (A–D) are exposed on the plate. In each set, the two gratings only partially overlap so they can be characterized both separately and as a multiplexed pair.

However, toward the goal of applying multiplexed gratings to spectral applications, we then characterized the multiplexed pair by fixing the input angle and varying the input wavelength. The experimental setup for for this characterization is depicted schematically in Fig. 3.4. The source in this case consisted of a Bausch and Lomb grating monochromator with a tungsten lamp. Imaging optics were included after the output slit of the monochromator to approximate a plane

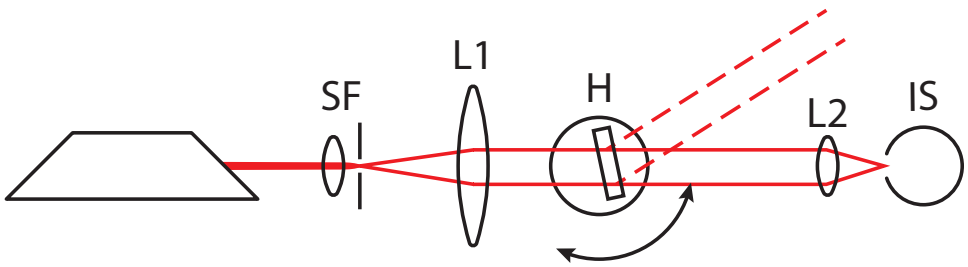

Figure 3.3: Experimental setup for hologram readout versus incident angle. The HeNe laser source is sent through a spatial filter (SF) and collimated with lens L1. The beam then passes through the holographic plate (H) which is mounted on a rotation stage. Each output order from the grating is individually focused by lens L2 into an integrating sphere with a built-in silicon photodetector (Thorlabs S140C).

wave at the holographic grating, and a polarizer was inserted to linearly polarize the light perpendicular to the plane of incidence with the holographic plate. The monochromator's input and output slit widths were set to provide a half-power output bandwidth of 5nm.

For measurements with either the 632nm source or the monochromator, we calculated diffraction efficiency values as the ratio of output power for a given diffraction order to input power. The power measurements were made with a ThorLabs S140C silicon photodetector and integrating sphere assembly. The measurements were then mathematically corrected to account for power loss due to Fresnel refraction at the glass surfaces. Reported diffraction efficiency values, therefore, follow the theoretical model in which Fresnel refraction is not considered.

Once each grating of a pair was characterized individually, its modeled parameters were adjusted to match the experimental data. The period and tilt of a grating and the local thickness of the holographic material vary from anticipated

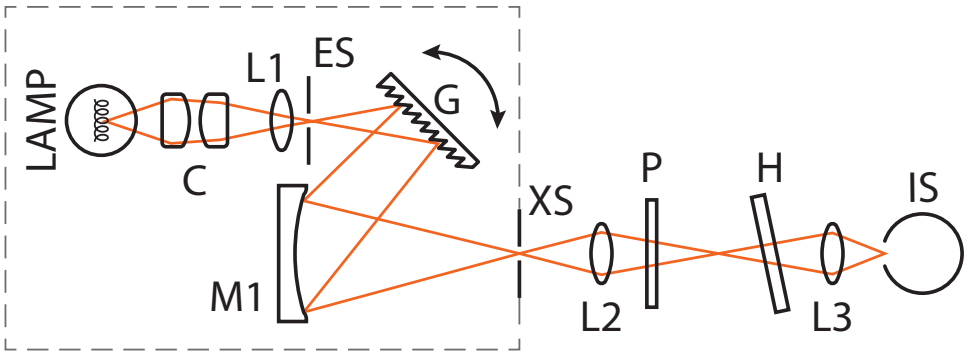

Figure 3.4: Experimental setup for hologram readout versus wavelength. The Bausch and Lomb grating monochromator (dashed box) consists of a tungsten lamp and condensing optics (C) the output of which is focused onto the entrance slit (ES) by lens L1. The diffraction grating (G) disperses the incident light, and rotating the grating determines which wavelength band passes through the exit slit (XS) after reflecting off of curved mirror M1. Lens L2 relays the monochromator output, linearly polarized by P, to the holographic plate (H). While not depicted, in practice the distance between lens L2 and the holographic plate is approximately 0.5m, so the wavefront at H is approximately planar over the grating area. Each output order from the grating is individually focused by lens L3 into the integrating sphere.

values due to gelatin shrinkage during development, and the final index modulation of a given grating is somewhat unpredictable. This experimental variability is effectively eliminated by adjusting the model to match 1) measured values for the peak diffraction efficiency, 2) the two incidence angles at which diffraction efficiency peaks occur at the measurement wavelength, and 3) the input angles corresponding to the first zeros of the diffraction efficiency curve.

After the single grating models' parameters are adjusted to fit experimental data as a function of input angle, the multiplexed model is recalculated for a fixed input angle but variable wavelength. These theoretical curves are then compared to experimental measurements of the multiplexed gratings without further adjustment. Not only is the initial single-grating characterization versus input

angle more straightforward experimentally, comparing data against both input angle and wavelength variation further reinforces the validity of the mathematical model.

3.4 Results

The experimental results for two different grating-pair designs are given in the following sections. The first pair exhibits cross-coupling interference. The second pair is similar, but Grating 2's construction angles were adjusted to eliminate the interference. This second pair is used as a control to ensure all of the gratings are operating in a linear region of the material.

3.4.1 Interfering Gratings

Characterizing the individual gratings of the interfering pair and feeding this data back into the model resulted in Fig. 3.5 plotting diffraction efficiency versus input angle for Grating 1 and a similar plot (not shown) for Grating 2. The solid curve represents the adjusted model, and the measured data points are superimposed. An expanded and collimated beam from a 632.8nm He-Ne laser was the light source. The gratings' defining parameters determined from the data fit are given in Table 3.1.

When the interfering multiplexed pair is characterized as a function of input wavelength, the diffraction efficiency curves appear as in Fig. 3.6. The solid curves are theoretical data from the model, and measured data points for each diffracted

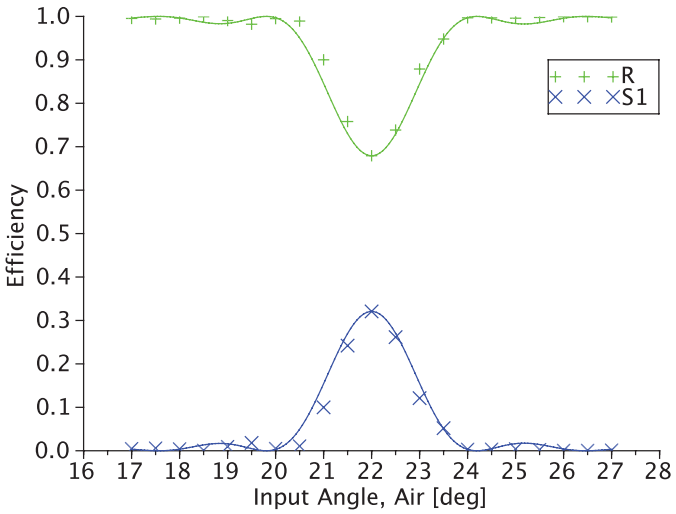

Figure 3.5: Diffraction efficiency of Grating 1 as a function of input angle for an input wavelength of 632.8nm. Solid lines show the theoretical efficiency after adjusting the model to fit the measured data.

	Grating 1	**Grating 2**
Bragg Angle 1 [deg., air at 632.8nm]	22.00	18.92
Bragg Angle 2 [deg., air at 632.8nm]	-31.17	-31.17
Period [μm]	0.71	0.75
Index Modulation, n_1	0.0040	0.0040
Thickness, d **[μm]**	29.0	29.0

Table 3.1: Parameters of the interfering grating pair determined by fitting the theoretical model to measured diffraction efficiency data.

wave are superimposed. The lighter dashed curves show what the S-wave diffraction efficiency of each grating would be if the other grating were not present.

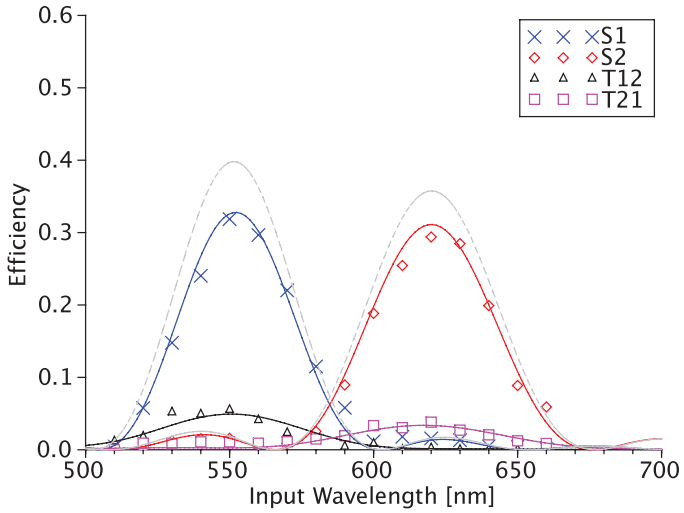

Figure 3.6: Diffraction efficiency of the significant output waves of the interfering grating pair as a function of input wavelength for an input angle (in air) of 18.5 degrees. Measured data is superimposed on theoretical data. The lighter dashed curves indicate what the S-wave diffraction efficiency of each grating would be if the other grating was not present in the holographic element.

Note that the experimental data matches quite well with the theory. There is a significant decrease in peak diffraction efficiency for each grating, and the two cross-coupled waves appear as expected. The cross-coupled waves are given unique symbols T_{12} and T_{21} corresponding to vectors $\boldsymbol{\tau}_{12} = \boldsymbol{\rho} - \boldsymbol{K}_1 + \boldsymbol{K}_2$ and $\boldsymbol{\tau}_{21} = \boldsymbol{\rho} + \boldsymbol{K}_1 - \boldsymbol{K}_2$.

	Grating 1	Grating 2
Bragg Angle 1 [deg., air at 632.8nm]	22.00	18.92
Bragg Angle 2 [deg., air at 632.8nm]	-31.17	-39.50
Period [μm]	0.71	0.66
Index Modulation, n_1	0.0043	0.0046
Thickness, d **[μm]**	29.0	29.0

Table 3.2: Parameters of the non-interfering grating pair determined by fitting the theoretical model to measured diffraction efficiency data.

3.4.2 Non-interfering gratings

To further reinforce that the above results are due to the physics of a multiplexed grating pair and not the result of non-linear material effects, a second, similar grating pair was constructed. This second pair was modified from the first to eliminate the occurrence of cross-coupled waves while keeping similar modulation levels for each grating. Specifically, the operating angles of the second grating were modified to detune the cross-coupling with the first grating.

Again the individual gratings were characterized as a function of input angle at a fixed wavelength, and the model parameters were adjusted to fit the experimental data. The resulting grating parameters for the non-interfering pair are given in Table 3.2. Note that the gratings' index modulation values in this case are actually slightly higher than for the interfering grating pair discussed above.

Plotting the adjusted model as a function of input wavelength results in the solid curves of Fig. 3.7, and again experimental measurements are superimposed.

Note that as in Fig. 3.6, the gratings non-multiplexed efficiency curves are included, but cannot be seen in the plot because they lie directly behind the multiplexed efficiency curves. That is, there is no significant expected change in S-wave diffraction efficiency and no appearance of T-wave (cross-coupled) efficiency resulting from multiplexing this grating pair for this wavelength range and input angle. Also note the good fit of the experimental data with the theoretical curves. We would expect the experimental data to deviate from theory if our exposures were saturating the holographic material. This reinforces that the results of Fig. 3.6 are not due to non-linear effects of the material.

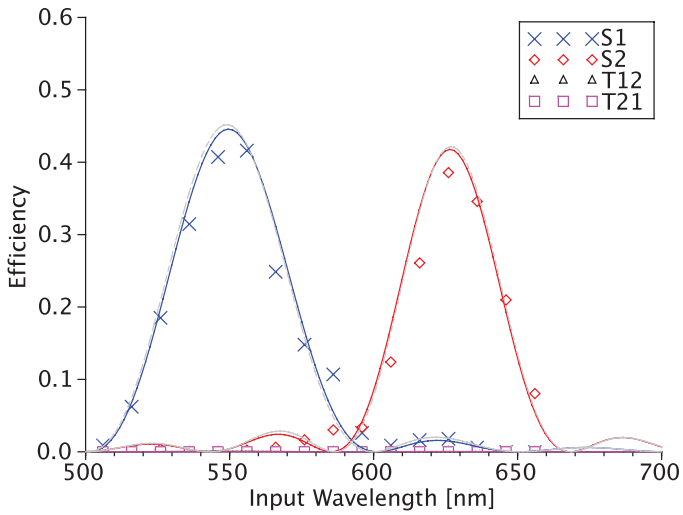

Figure 3.7: Diffraction efficiency of the significant output waves of the non-interfering grating pair as a function of input wavelength for an input angle (in air) of 18.5 degrees. Measured data is superimposed on theoretical data.

Although the mathematical method developed in Chapter 2 is suitable for analyzing diffraction efficiencies as a function angle of incidence or input wavelength, the focus here has been on variations of the input wavelength. The experimental

data in this chapter with broadband two-grating holographic elements confirms the theory, and this method can now be applied to optimization algorithms for solar spectral splitting (Chapter 4), spectral beam-combining (Chapter 5), and other spectral systems utilizing multiplexed volume Bragg gratings.

Chapter 4

Multi-grating Systems for Solar Spectrum Splitting

In this chapter we explore the application of multiple volume Bragg gratings (VBGs) to optimize the performance of spectral bandpass filters especially with regard to minimizing dispersion. Section 1.1 introduced the concept of solar spectrum splitting systems for improved power generation efficiency in photovoltaic (PV) cells. Poor matching between semiconductor bandgap energies and incident photon energies is a key source of inefficiency in these systems. By employing multiple PV cells with bandgaps tailored to subsets of the incident spectrum, this inefficiency can be partially mitigated. To do this requires either heterogeneous bandgap semiconductors [12] or an efficient spectrum splitting optical system. The work in this chapter is related to the latter.

In the first section, we discuss three different types of holographic spectrum

splitters: single-gratings, sandwiched-gratings, and multiplexed-gratings. We include their qualitative differences and describe methods for quantifying their performance. Then in Section 4.2 we use a heuristic algorithm to optimize these systems and compare their performance under various constraints.

While we do not consider optical concentration (focusing) or performance over a range of input angles, techniques similar to those presented here could be applied to optimizing systems incorporating these additional features into their HOEs. Further, although the filter efficiencies we show in the following sections are somewhat lower than those of simple dichroic filters, additional features such as concentration are often inherently simpler to incorporate with an all-transmissive system.

4.1 Multi-grating Volume Holographic Spectrum Splitters

Use of a spectrum splitter of any kind is motivated by the need to better match PV-cell bandgap energies with portions of the incident spectrum. The typical method of calculating ideal conversion efficiency (i.e. absent absorption losses, reflection losses, etc.) assumes that photon energies $E_{\text{photon}} = hc/\lambda_{\text{photon}}$ that do not exceed the PV cell bandgap energy $E_{\text{gap}} = hc/\lambda_{\text{gap}}$ are unusable by the system. On the other hand, photons with energy exceeding the bandgap energy contribute only the bandgap energy to the system, and all excess energy is lost. Thus, conversion efficiency in an ideal PV cell, η_{cell}, is linear with incident wavelength for photon

energies greater than the bandgap energy and zero otherwise:

$$\eta_{\text{cell}}(\lambda_{\text{photon}}) = \begin{cases} \lambda_{\text{photon}}/\lambda_{\text{gap}}, & \text{if } \lambda_{\text{photon}} \leq \lambda_{\text{gap}} \\ 0, & \text{otherwise} \end{cases} \tag{4.1}$$

The efficiency advantage of employing additional bandgaps and a spectrum splitter in a solar power generation system can be illustrated as follows. Two bandgaps are arbitrarily placed at 1.38eV ($\lambda_{\text{gap1}} = 900\text{nm}$) and 0.50eV ($\lambda_{\text{gap2}} = 2500\text{nm}$) as shown in Fig. 4.1. If one integrates the solar spectral irradiance over the plotted wavelengths, the total irradiance is roughly 790W/m^2. When idealized conversion efficiency is assumed and only the larger bandgap is employed, the converted power is approximately 360W per unit area (45.6%), and if only the smaller bandgap is employed, the converted power is approximately 290W per unit area (36.7%). However, if both bandgaps are employed in a system with an ideal spectrum splitter (i.e. wavelengths greater than λ_{gap1} are exclusively directed onto the larger bandgap PV cell), converted power per unit area increases to approximately 520W (65.8%).

Given that employing an additional bandgap increases the power conversion potential of a system, we turn our attention to the efficiency of spectrum splitters consisting of one or more volume Bragg gratings (VBGs). The baseline case is that of a single VBG designed such that shorter incident wavelengths are diffracted strongly and redirected onto the system's large bandgap PV cell, while longer wavelengths are allowed to pass through the VBG to the small bandgap PV cell.

Flexibility in the parameters defining a VBG (i.e. the wavelength and angle

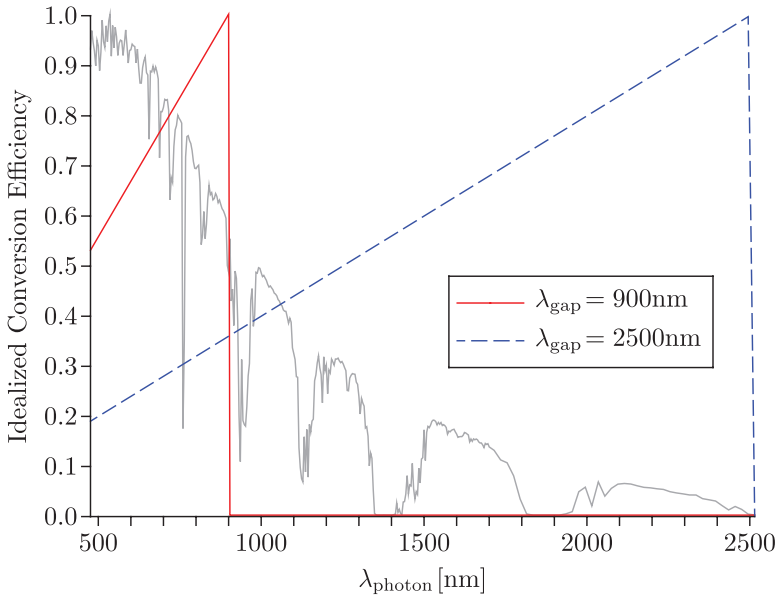

Figure 4.1: Conversion efficiency for two different PV cell bandgap energies ($E_{\text{gap}} = hc/\lambda_{\text{gap}}$) as a function of incident photon wavelength, λ_{photon}, (after [41]). For photon energies exceeding the bandgap energy (i.e. $\lambda_{\text{photon}} \leq \lambda_{\text{gap}}$), only energy up to the bandgap energy is converted, so conversion efficiency is linear reaching (ideally) 100% for $\lambda_{\text{photon}} = \lambda_{\text{gap}}$. Conversion efficiency is zero for photon energies below the bandgap energy. The efficiency curves are superimposed over the (normalized) direct-incidence solar spectral irradiance curve [42] for reference.

pairs resulting in Bragg resonance) allows the engineer to tailor the spectral response of the grating as well as the nominal output angle for the diffracted band. However, VBGs suffer from two shortcomings when applied in broadband applications such as spectrum splitting. First, the main lobe of the grating's diffraction efficiency curve as a function of wavelength (see e.g. Figure 4.4) is a relatively poor approximation to an ideal bandpass filter. Second, the range of output angles as a function of wavelength can be quite large over a wide spectral band (i.e. there is significant dispersion). The first issue simply limits the overall efficiency of the filter and therefore the total power conversion efficiency of the system. The second issue restricts the placement and minimum sizes of PV cells required to completely collect the diffracted light.

Both of these issues can be addressed in part through the inclusion of additional VBGs in the two-band system. The additional gratings are used to improve the diffraction efficiency and dispersion characteristics of the spectrum splitter, allowing its performance to better approximate an ideal bandpass filter. However, the inclusion of a second grating introduces inter-grating interference effects (i.e. cross-coupling) that reduce efficiency in diffracted orders of interest and result in additional diffracted orders that lead to stray light in the system.

We explore two arrangements of multi-VBG spectrum splitters: sandwiched gratings and multiplexed gratings. In both cases, we seek a combined grating structure that diffracts the high-energy band of the incident spectrum toward the large bandgap semiconductor with high efficiency and low dispersion.

4.1.1 Sandwiched-grating Systems

The sandwiched arrangement is depicted schematically for two gratings in Fig. 4.2. Separate holographic elements are used for each grating, and they are placed in series in the optical path. The system accepts broadband incident light from one direction (here assumed to be normal to the top element). Characteristically, a volume Bragg grating has a single diffraction order, so for a particular incident wavelength, some portion of the incident light is diffracted by the first grating (G1) toward the large bandgap semiconductor (order S_1'), and the undiffracted light remains in order R'. Both R' and S_1' then interact with the second grating (G2) where they are each split into two diffraction orders resulting in the final four orders of interest: R, S_1, S_2, and T_{12}. Additionally, the three diffracted orders are dispersed by the gratings. Also note that if the sequence of the gratings is reversed, the T_{12} order will be replaced by a different T_{21} order and the relative efficiencies of the four output orders will change. We show in Section 4.2.2 that for the conditions under consideration here, performance can be improved slightly by placing the grating G1 (which affects primarily shorter wavelengths) first in the sequence.

Calculating diffraction efficiency of each diffracted order of interest in a sandwiched-grating system involves a straightforward application of the well-known coupled-wave method of Kogelnik in multiple stages. To summarize the method for a single phase grating, it is typical to assume that two significant waves are present in the HOE which results in the following coupled differential equations (see also

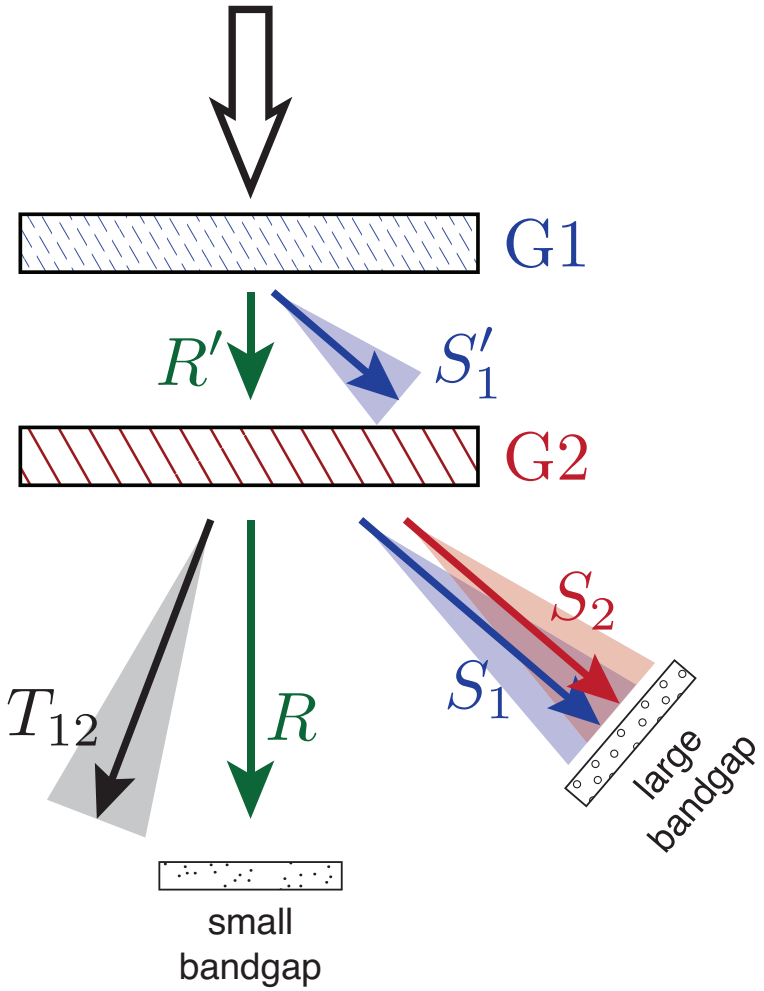

Figure 4.2: Input and output orders and PV cell locations for a notional two-grating sandwiched system. Broadband light enters normal to the holographic elements from above. For a particular wavelength, Grating 1 (G1) splits the incident light into an undiffracted (R') and a diffracted order (S_1'). R' is then split by Grating 2 (G2) into orders R and S_2. Grating 2 also splits S_1' into the S_1 (undiffracted) and T_{12} (diffracted) orders. Each diffracted order is also dispersed. (The gratings are shown separated in order to highlight the intermediate diffracted orders. Typically there would be no space between the two HOEs.)

Chapter 2):

$$c_R \frac{dR}{dz} = j\kappa S \tag{4.2a}$$

$$c_S \frac{dS}{dz} - j\vartheta S = j\kappa R \tag{4.2b}$$

where R and S refer to the complex amplitudes of the zero-order and diffracted-order waves respectively and are functions of z, the distance traveled through the HOE. κ is a function of the index modulation of the grating and the operating wavelength, and c_R and c_S are the direction cosines of the respective waves. ϑ is a function of the vector combination of the input wavevector and the grating vector and the operating wavelength. When the input is Bragg-matched with the grating, $\vartheta = 0$, and the diffraction efficiency of the grating is maximized. This peak diffraction efficiency of the grating can be as high as 100% for a transmission-mode grating, and the diffraction efficiency falls off from this peak value when the Bragg condition is violated (or $\vartheta \neq 0$) by changes in the input angle and/or wavelength.

For a given incident wavelength at a given input angle, the relative powers of the diffracted and undiffracted orders of the first grating in the sandwiched spectrum splitter are calculated by solving Eq. 4.2 with appropriate boundary conditions. Additionally, the output angle of the diffracted order—which is also a function of input angle and wavelength—is calculated [43]. The relative powers and calculated angles are then fed forward into similar calculations for the second and any subsequent gratings in the sandwich resulting in a multitude of output orders at known angles and with a known relative power distribution. This process

is repeated for the orthogonal polarization and the results are averaged under the assumption that the incident spectrum is randomly polarized. This entire process is then repeated for other wavelengths of interest across the input spectrum.

For a two-grating, two-bandgap system, ideally all of the wavelengths from the high-energy portion of the incident spectrum (i.e. $\lambda_{\text{photon}} \leq \lambda_{\text{gap1}}$) would be diffracted into either order S_1 or S_2 where they would impinge on the large bandgap semiconductor. The wavelengths in the low-energy portion of the incident spectrum would remain in order R and would impinge on the small bandgap semiconductor. However, like the single-grating system, some high-energy photons remain in order R simply because the gratings' diffraction efficiencies are, in general, less than 100% for the wavelengths and polarizations of interest. Also, as in the single-grating system, dispersion of the diffracted order(s) can result in light that physically misses the large bandgap PV cell and is lost. Unlike single-grating systems, sandwiched-grating systems exhibit additional loss due to high-energy photons directed toward the large bandgap cell by one grating being diffracted again by a subsequent grating into an unusable direction (cross-coupled orders, T_{mn}). This cross-coupling loss is exacerbated by the addition of more gratings in the sandwich.

4.1.2 Multiplexed-grating Systems

In the multiplexed-grating arrangement shown in Fig. 4.3, two volume Bragg gratings are combined into a single holographic element. The system accepts broadband incident light from one direction. For a given incident wavelength,

light from this input that is not diffracted by the gratings (the R order) passes through the holographic element and is incident on the small bandgap PV cell. The two gratings' directly-coupled orders (S_1 and S_2) are diffracted toward the large bandgap PV cell. Like the sandwiched-grating system from Section 4.1.1 there are also cross-coupled orders (T_{mn}), and all diffracted orders are dispersed.

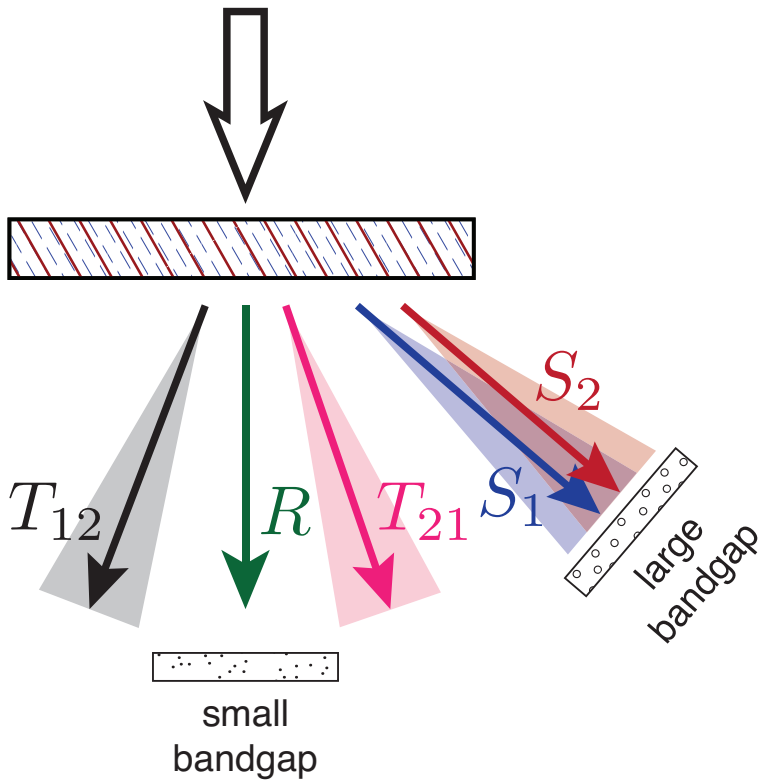

Figure 4.3: Input and output waves and PV cell locations for a two-grating multiplexed system. Broadband light enters normal to the holographic element from above. Undiffracted light (R) is incident on the small bandgap PV cell. Directly-coupled light from each grating (S_1 and S_2) is dispersed and is nominally incident on the large bandgap PV cell. Cross-coupled light (T_{12} and T_{21}) is dispersed and is assumed to not be incident on either cell.

Unlike the sandwiched-grating system, though, a two-grating multiplexed system will have (at least) two cross-coupled orders (T_{12} and T_{21}) as opposed to just

one cross-coupled order in the two-grating sandwiched system. The additional cross-coupled order arises because the two gratings in the HOE must be treated simultaneously. For a single grating, the single diffracted wave arises from the vector combination of the input wavevector and the grating vector. For multiplexed gratings, additional diffracted waves arise from vector combinations of the input wavevector and permutations of one or more grating vectors. Mathematically, these additional waves give rise to a larger set of coupled differential equations similar to Eq. 4.2 that must be solved simultaneously.

In addition to the presence of the cross-coupled orders themselves, the complex coupling relationships among the various significant waves result in inter-grating interference effects including reduced peak diffraction efficiency in directly-coupled orders and shifts in the angle and wavelength combinations that result in peak diffraction efficiency. We discussed these interference effects and a method for calculating diffraction efficiencies in HOEs with multiplexed gratings in Chapter 2.

Given the complicated relationships among multiple direct- and cross-coupled orders in sandwiched-grating and especially multiplexed-grating spectrum splitters, design of HOEs for these systems is a non-intuitive exercise. In order to compare the relative performance of these classes of holographic spectrum splitters, we employ a heuristic optimization algorithm in the next section.

4.2 Spectrum Splitter Optimization

Designing a holographic spectrum splitter comprised of one or more volume Bragg gratings in any arrangement is a problem of many dimensions. To compare the

relative performance of the different grating arrangements discussed in Section 4.1, we require a method of maximizing the performance of a given arrangement. To this end, we employ a particle swarm optimization (PSO) algorithm [44] that searches the parameter space of a particular grating arrangement and seeks to maximize the power conversion efficiency of the two bandgap spectrum splitting system.

Particle swarm optimization was originally devised based on artificial life models of fish schooling and bird flocking. Individuals in the school or flock explore a space for a position that maximizes some value function (e.g. a good source of food). Each individual in the swarm knows the best location it has encountered so far as well as the overall best location encountered by any individual in the swarm. An individual's motion from one point in time to the next is randomized but also tends to draw the individual toward these best known positions. In general, PSO randomly populates a multi-dimensional search space with a set of particles, the values of the particle positions are calculated based on some metric unique to the problem at hand, and the particles' velocities (and thus positions) are updated based on the best known positions. This process continues iteratively until some convergence criterion is achieved or an iteration limit is reached.

To set up our PSO algorithm, we first define the search space. The variables defining a non-concentrating, multi-grating spectrum splitter include input and output angles, grating thicknesses, center wavelengths for each grating, and index modulation values for each grating. For the optimization results presented in this section, we assume a constant input angle normal to the grating (i.e. $\theta_{in} = 0°$). The output angles of the constituent gratings are kept equal to each other, and

this output angle of the system, θ_{out}, is allowed to vary between 15° and 35° in air assuming a bulk index of refraction of $n = 1.55$.

By definition, the thicknesses of the constituent gratings in a multiplexed-grating HOE are equal. To better compare performance between multiplexed- and sandwiched-grating spectrum splitters, we also keep the thicknesses of the sandwiched arrangement's constituent HOEs equal although these could vary independently in practice. A multiplexed-grating spectrum splitter, then, has a total thickness of d, and a two-grating sandwiched spectrum splitter has a total thickness of $2d$, where d is varied by the optimizer between 15 and 60μm.

We keep the bandgaps of the two PV-cells constant throughout our optimization because these values are usually dictated by the nature of the semiconductors used. As in the discussion of Section 4.1, we use bandgaps corresponding to wavelengths $\lambda_{\text{gap1}} = 900\text{nm}$ and $\lambda_{\text{gap2}} = 2500\text{nm}$. The high energy band is defined between 475 and 900nm for calculation purposes. For a system of N gratings, this band is subdivided into N equal sub-bands, and the optimizer varies the center wavelength, λ_i, of each grating over the respective sub-band. Note that with our focus on the spectrum splitter itself, the bandgaps were simply chosen as round figures in terms of wavelength that suit salient features of the incident spectrum. However, the bandgap energies, 1.38eV and 0.50eV, do roughly correspond with the bandgap energies of Gallium (III) Arsenide (1.43eV at 300K) and Germanium (0.66eV at 300K) respectively [45].

Finally, the index modulation value, n_{1i}, of each grating is varied by the optimizer and is limited to ±2% of the value which would give the grating 100%

diffraction efficiency for s-polarized light at its defined center wavelength if operating in isolation. By varying this parameter, the optimizer can improve system performance in the presence of inter-grating coupling effects and under the assumption of random input polarization (i.e. efficiency values are calculated for both s-polarization and p-polarization, and the results are averaged).

A spectrum splitter consisting of N gratings, then, is described by $(2N + 2)$ variables. Each grating has two associated variables, λ_i and n_{1i}, and the system as a whole has two additional variables, θ_{out} and d. The particle swarm optimizer is initialized by uniformly distributing 120 particles in this $(2N + 2)$-dimensional space and setting the velocity of each particle to 0. The PSO algorithm tracks the particles' best known positions through a metric based on the fixed bandgap energies, the solar spectrum, and the diffraction efficiencies of the constituent gratings of the system. For each wavelength of interest in the solar spectrum, the solar spectral irradiance[1], $I_{\text{solar}}(\lambda)$, is multiplied by the zero-order "efficiency" of the grating(s), $\eta_0(\lambda)$, and the smaller bandgap energy and is divided by the photon energy, $E(\lambda)$. This results in the effective irradiance collected and converted by the smaller bandgap PV cell for that wavelength:

$$I_{\text{gap2}}(\lambda) = \frac{I_{\text{solar}}(\lambda)\eta_0(\lambda)E_{\text{gap2}}}{E(\lambda)} \tag{4.3}$$

For wavelengths smaller than the high-energy bandgap limit, the first-order diffraction efficiencies of each grating, η_{1i}, are used in a similar fashion to determine the effective irradiance collected and converted by the larger bandgap PV cell for each

[1]Here I is used for spectral irradiance rather than the conventional $E_{e,\lambda}$ to avoid confusion with E for energy.

wavelength:

$$I_{\text{gap1}}(\lambda) = \sum_{i=1}^{N} \frac{I_{\text{solar}}(\lambda)\eta_{1i}(\lambda)E_{\text{gap1}}}{E(\lambda)} \tag{4.4}$$

The solar spectrum is divided into 150 bins and these equations are used to calculate the metric for each particle in the swarm as the ratio of total effective irradiance to available irradiance:

$$\Omega = \frac{\sum_{j=1}^{150} I_{\text{gap1}}(\lambda_j) + I_{\text{gap2}}(\lambda_j)}{I_{\text{available}}} \tag{4.5}$$

For each iteration, Ω for each particle is calculated using Eq. 4.5 and the largest values of this metric discovered for each particle and for the swarm as a whole are tracked. Then each particle's velocity vector is updated via:

$$\boldsymbol{v}_{n+1} = \omega \boldsymbol{v}_n + \phi_p r_p \boldsymbol{\Delta}_{p,best} + \phi_g r_g \boldsymbol{\Delta}_{g,best} \tag{4.6}$$

and each particle's position vector is updated via:

$$\boldsymbol{p}_{n+1} = \boldsymbol{p}_n + \boldsymbol{v}_{n+1} \times (1 \text{ iteration}) \tag{4.7}$$

where ω, ϕ_p, and ϕ_g are tuning constants for the simulation, $\boldsymbol{\Delta}_{p,best}$ and $\boldsymbol{\Delta}_{g,best}$ are the vectors between the given particle and the particle's and swarm's (respectively) best known positions, and r_p and r_g are uniformly-distributed random numbers between 0 and 1 that are updated for each calculation. Parameter limits are enforced by setting elements of a particle's new position vector that exceed the defined limits of the search space to the nearest boundary value and setting the

corresponding element of the particle's velocity vector to 0.

Given finite execution time, PSO does not guarantee finding the the global optimum. However, by adjusting the simulation variables ω, ϕ_p, and ϕ_g, the convergence of the simulation can be adjusted to avoid converging too quickly to a local extremum and also to avoid converging too slowly in general. Examining Eq. 4.6, ω is analogous to the particle's inertia, and ϕ_p and ϕ_g are analogous to gravity pulling the particle toward the particle's and swarm's best known positions. The values of these variables were determined through experimentation and are initialized in the optimizer to 0.75, 0.40, and 0.04 respectively. The optimizer runs for 100 iterations which was shown to be sufficient to give consistent results over repeated trials. After 66 iterations the simulation variables are changed to 0.65, 0.35, and 0.10 respectively to accelerate convergence to the swarm's best known position and increase the number of particles in the vicinity of that position to fine tune the result.

Results obtained by using this algorithm to optimize different types of solar spectrum splitting systems are given in the following sections. In addition to the relative performance of the different system types, we explore the impact of constraining dispersion of the diffracted orders in the system.

In Section 4.2.1 we optimize a single grating spectrum splitter assessing both efficiency and dispersion performance. This single grating is then optimized again after applying a constraint under which only diffracted wavelengths that exit the HOE within $\pm 2^\circ$ of the splitter's nominal output angle, θ_{out}, are included in the particle swarm metric calculations. Then we show how efficiency performance can be improved under the same dispersion constraint by adding a second grating to

the system in either a sandwiched (Section 4.2.2) or multiplexed (Section 4.2.3) arrangement. Finally, in Section 4.2.4 we show how adding a third grating can be advantageous under an even more stringent dispersion constraint.

4.2.1 Single Grating

The diffraction efficiency as a function of input wavelength of a single volume Bragg grating spectrum splitter is shown in Fig. 4.4. This single grating performs reasonably well allowing conversion of 57.6% of the available power. (Recall that an ideal bandpass filter would allow conversion of 65.8% of available power.) However, the dispersion over the high-energy band (475–900nm) is quite large, spanning approximately 10.5° as shown in Fig. 4.5.

Practical cell designs often require an angular range far smaller than that exhibited by this single grating. To that end, we optimize the system again adding an arbitrary limit to the allowed dispersion: only diffracted light exiting the system within ±2° of the nominal angle toward the large bandgap PV cell is included in converted energy calculations. Diffracted light outside this limit is assumed to be lost.

Diffraction efficiency results for the dispersion-constrained single-grating spectrum splitter are shown in Fig. 4.6. The gray band superimposed on the plot indicates the wavelengths meeting the dispersion constraint. In this case, the system is only capable of converting 51.0% of the available power.

Note that the wavelengths with the highest corresponding grating diffraction efficiency do not correspond with the highest values in the solar spectral irradiance

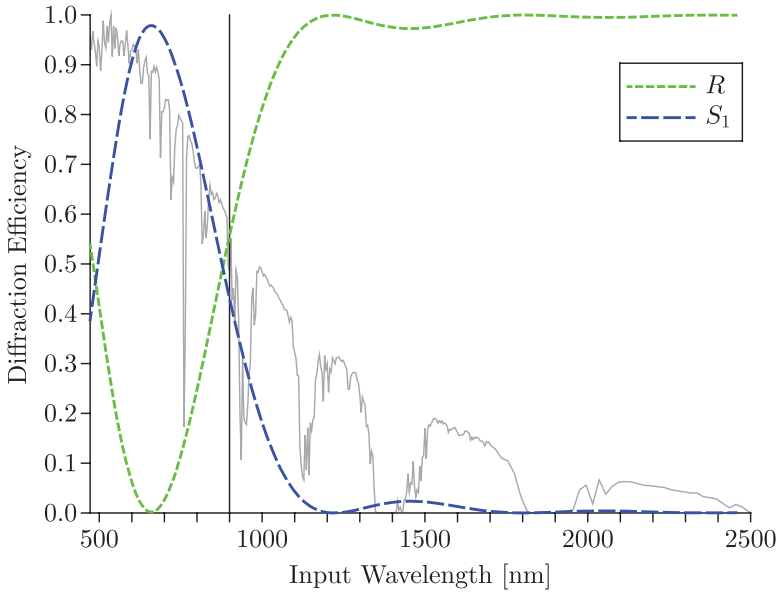

Figure 4.4: First-order (S_1) and zero-order (R) diffraction efficiency as a function of wavelength for a single volume grating spectrum splitter superimposed over the (normalized) solar spectral irradiance. The vertical line at 900nm indicates the longest wavelength absorbed by the large bandgap PV cell. This grating was optimized without limiting allowed dispersion.

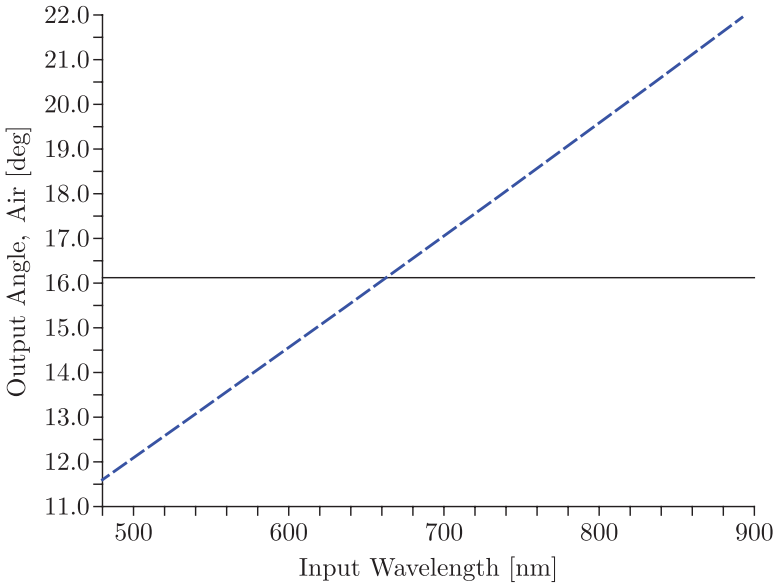

Figure 4.5: Dispersion of the diffracted order for a single volume grating spectrum splitter over the high-energy wavelengths of interest. The horizontal line indicates the nominal diffracted output angle of the system.

curve. Some shorter wavelengths exhibit higher spectral irradiance, but due to the difference between the corresponding photon energies and the large bandgap energy, the overall system is actually more efficient if the slightly lower energy photons are diffracted toward the large bandgap PV cell.

Also note, comparing Fig. 4.4 and Fig. 4.6, that the width of the main lobe of the S_1 diffraction efficiency curve is significantly reduced when dispersion is constrained. This is the result of the optimizer selecting a thicker holographic material (55.5μm versus 29.2μm) for the latter case. Due to the dispersion in the single-grating system, it is advantageous to narrow the diffraction band in this way, allowing more incident light to pass through to the small bandgap PV cell rather than diffracting this light into a widely dispersed order where much of it misses the large bandgap cell.

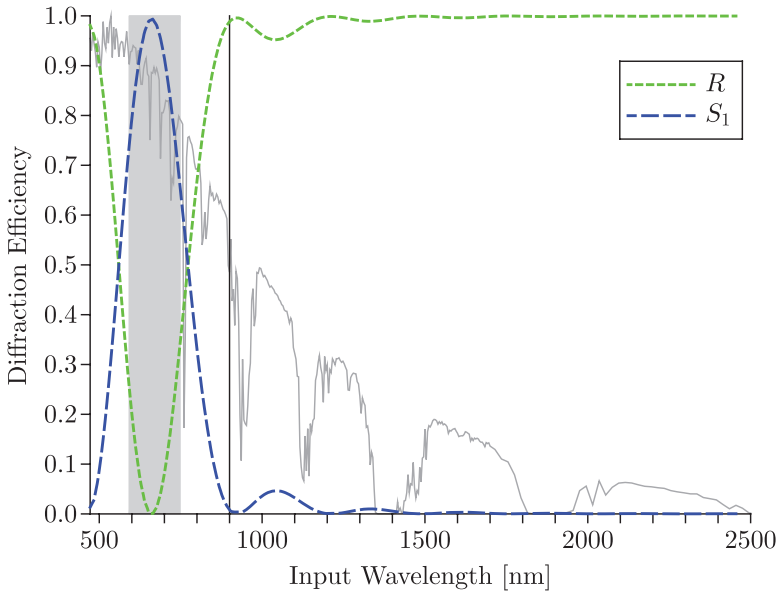

Figure 4.6: First-order (S_1) and zero-order (R) diffraction efficiency as a function of wavelength for a single volume grating spectrum splitter superimposed over the (normalized) solar spectral irradiance. The vertical line at 900nm indicates the longest wavelength absorbed by the large bandgap PV cell. Dispersion was constrained when optimizing this grating. The gray band indicates the wavelength range meeting the dispersion constraint.

4.2.2 Two Sandwiched Gratings

It is clear from Fig. 4.6 that more incident light could be directed toward the large bandgap PV cell with the addition of a second grating. When this is implemented in a sandwiched-grating configuration (see Fig. 4.2), the optimized diffraction efficiencies appear as in Fig. 4.7 with gray bands again indicating the wavelength ranges that meet the dispersion constraint. The power conversion efficiency in this case increases to 54.0%. Here the gratings are sequenced such that incident light encounters grating 1 first. The conversion efficiency of the system is slightly lower (53.9%) if the optimizer is re-run with the gratings in the opposite sequence (not depicted) due to the differing nature of the cross-coupled order that appears (see Section 4.1.1).

When the second grating is added to the system, the two gratings each need to operate over only roughly half of the high-energy band. Further, the gratings are defined such that their center wavelengths (i.e. the wavelength at which peak diffraction efficiency occurs) exit the system at the same diffracted angle. This allows the dispersion to "reset" resulting in a smaller overall span of output angles as shown in Fig. 4.8. This angular overlap of the two gratings' diffracted orders allows for improved system performance under our applied dispersion constraint.

The optimizer selects similar values for the nominal output angle (here 16.6° in air) and holographic material thickness (here 58.7μm) when compared to the single-grating case. In general, dispersion in a volume grating is reduced as the difference between the incident and diffracted angles is reduced. However, the diffraction efficiency curves also tend to widen with respect to wavelength as this

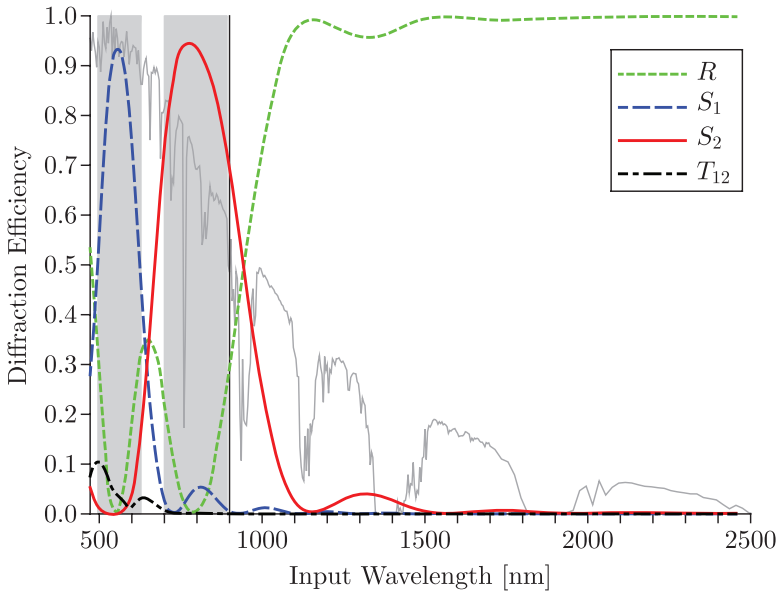

Figure 4.7: Zero-order (R), first-order (S_1 and S_2), and cross-coupled (T_{12}) diffraction efficiency as a function of wavelength for a sandwiched two-grating spectrum splitter superimposed over the (normalized) solar spectral irradiance. Incident light encounters grating 1 first. The vertical line at 900nm indicates the longest wavelength absorbed by the large bandgap PV cell. Dispersion was constrained when optimizing these gratings. The gray bands indicate the wavelength ranges meeting the dispersion constraint.

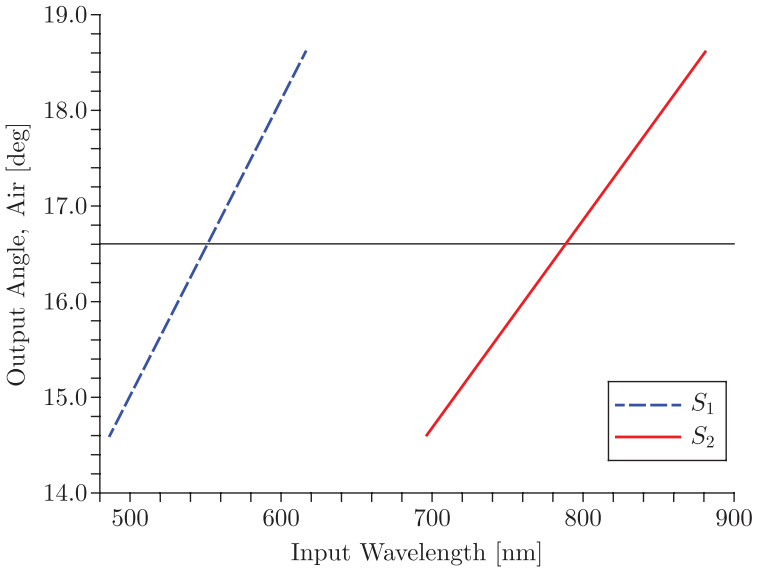

Figure 4.8: Dispersion of the first diffracted orders (S_1 and S_2) for a sandwiched two-grating spectrum splitter over the high-energy wavelengths of interest. The horizontal line indicates the nominal diffracted output angle of the system. Note how employing two gratings allows the output angles to overlap reducing the overall span.

angular difference is reduced. Widening the diffraction efficiency curves should lead to more loss in the system due to a) relatively high diffraction efficiency for wavelengths that do not meet the dispersion constraint, and b) increased cross-coupling interference. However, increasing the thickness of the holographic material counteracts this effect by narrowing the diffraction efficiency curves, and the optimizer tends to choose a material thickness that tailors the curves to the wavelength spans that fulfill the dispersion constraint.

4.2.3 Two Multiplexed Gratings

When the two gratings comprising the spectrum splitter are multiplexed into a single HOE (see Fig. 4.3) and optimized, the diffraction efficiency curves appear

as in Fig. 4.9. The power conversion efficiency, 53.2%, is lower than that of the sandwiched-grating arrangement due to several factors. Like the sandwiched-grating arrangement, the optimizer chose a relatively shallow output angle (20.2° in air) and relatively thick holographic material (58.2μm) again to tailor the regions of high diffraction efficiency to wavelength spans that fulfill the dispersion constraint. In the multiplexed-grating arrangement, though, the HOE is subject to additional cross-coupled orders. Both T_{12} and T_{21} are present (although the effect of the latter is quite small), and inter-grating interference effects cause a significant decrease in the peak diffraction efficiency of the S_1 order.

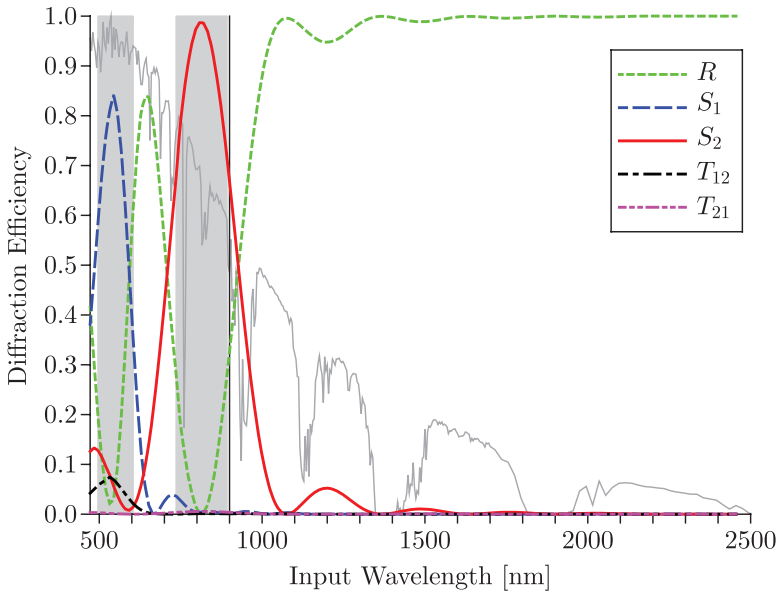

Figure 4.9: Zero-order (R), first-order (S_1 and S_2), and cross-coupled (T_{12} and T_{21}) diffraction efficiency as a function of wavelength for a multiplexed two-grating spectrum splitter superimposed over the (normalized) solar spectral irradiance. The vertical line at 900nm indicates the longest wavelength absorbed by the large bandgap PV cell. Dispersion was constrained when optimizing these gratings. The gray bands indicate the wavelength ranges meeting the dispersion constraint.

As shown in Fig. 4.10, the multiplexed-grating arrangement exhibits angular

overlap in its S_1 and S_2 diffracted orders in a similar fashion to the sandwiched-grating arrangement. This again results in a performance improvement over the single-grating case. Further, unlike the sandwiched-grating arrangement, the multiplexed system can be contained in a single HOE layer assuming the dynamic range of the holographic material is not exceeded through multiple exposures.

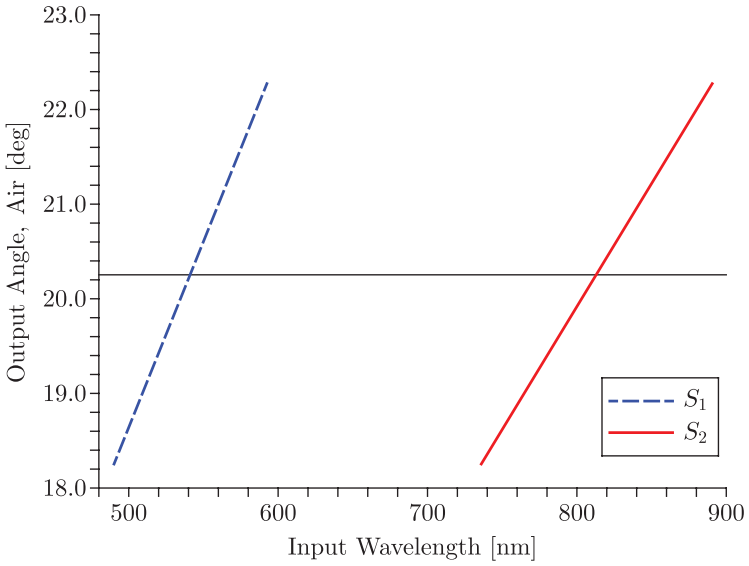

Figure 4.10: Dispersion of the first diffracted orders (S_1 and S_2) for a multiplexed two-grating spectrum splitter over the high-energy wavelengths of interest. The horizontal line indicates the nominal diffracted output angle of the system. Note how employing two gratings allows the output angles to overlap reducing the overall span.

4.2.4 Three Multiplexed Gratings

Finally, we explore the effect of a more stringent dispersion constraint on the spectrum splitting system, again optimizing the multiplexed-grating arrangement. If we reduce the output diffraction orders' allowed angular span to $\pm 1^\circ$ around the nominal output angle and optimize the system again, the power conversion

efficiency of the two-grating multiplexed system reduces to 48.8%.

It stands to reason that the system could better meet this new dispersion constraint by further subdividing the high-energy diffracted band through the inclusion of a third grating. When three gratings are multiplexed into a single HOE and optimized, the diffraction efficiency curves appear as in Fig. 4.11, and the output angles of the desired diffracted orders are shown in Fig. 4.12. Again, the diffracted orders exhibit overlap which helps to meet the dispersion constraint, but the power conversion efficiency of the system decreases to 45.9%. The peak diffraction efficiency of each of the gratings is significantly compromised due to inter-grating interference within the multiplexed HOE. These effects ultimately limit the efficacy of adding more gratings to this type of system to improve dispersion performance.

4.3 Conclusion

Employing multiple volume Bragg gratings can lead to improved performance in solar spectrum splitters over the use of a single VBG both in terms of overall system efficiency and in dispersion characteristics. These improvements can be seen in both sandwiched-grating and multiplexed-grating spectrum splitters. The former exhibits higher efficiency performance, while the latter has the advantage of utilizing only a single layer of holographic material. Optimized efficiency values and angular spans of dispersed outputs for each type of spectrum splitter explored in Section 4.2 are summarized in Table 4.1.

While neither sandwiched- nor multiplexed-grating spectrum splitters can match

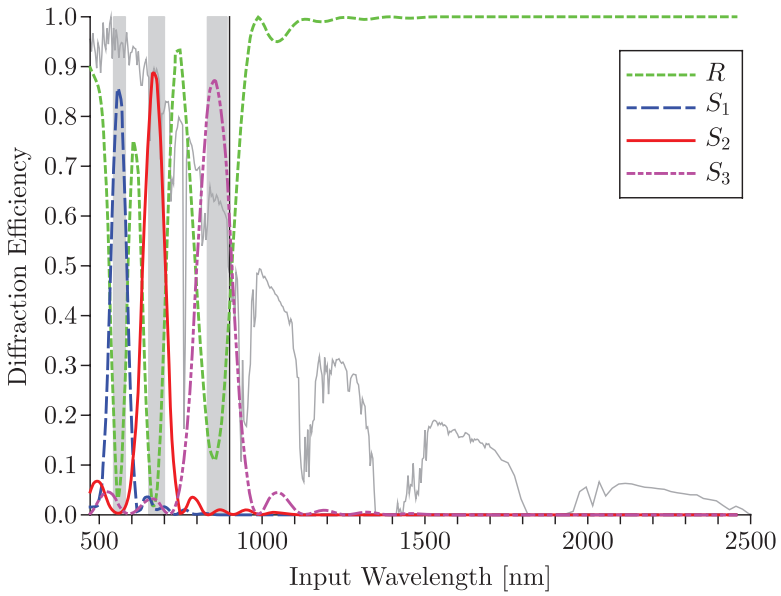

Figure 4.11: First-order for each grating (S_1, S_2, and S_3) and zero-order (R) diffraction efficiency as a function of wavelength for a multiplexed three-grating spectrum splitter superimposed over the (normalized) solar spectral irradiance. The vertical line at 900nm indicates the longest wavelength absorbed by the large bandgap PV cell. Output angles were constrained to $\pm 1^\circ$ around the nominal output angle when optimizing these gratings. The gray bands indicate the wavelength ranges meeting the dispersion constraint. Several cross-coupled orders, T_{mn}, are present but not depicted for clarity.

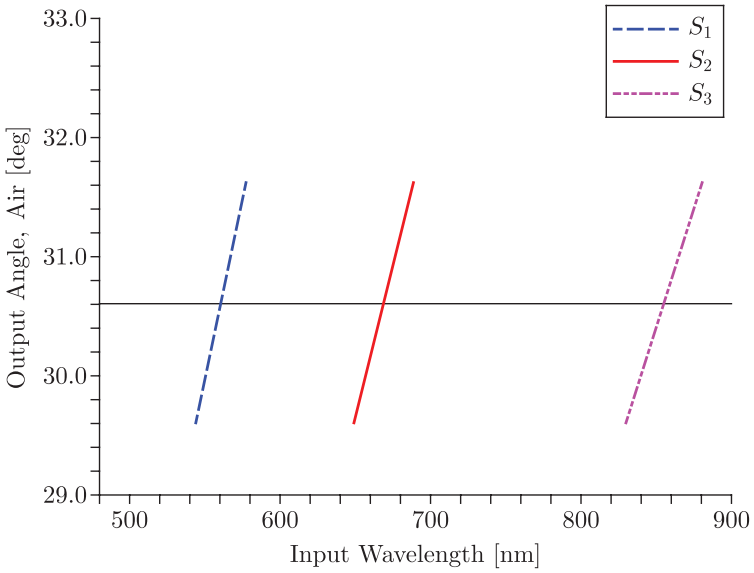

Figure 4.12: Dispersion of the first diffracted orders (S_1, S_2, and S_3) for a multiplexed three-grating spectrum splitter over the high-energy wavelengths of interest. The horizontal line indicates the nominal diffracted output angle of the system. Note the angular overlap of all three diffracted orders.

	Conversion Efficiency	**Dispersion Angular Span**
Ideal Bandpass Filter	65.8%	–
1 Grating, unconstrained dispersion	57.6%	±5.3°
2 Sandwiched Gratings	54.0%	±2.0°
2 Multiplexed Gratings	53.2%	±2.0°
1 Grating	51.0%	±2.0°
2 Multiplexed Gratings	48.8%	±1.0°
3 Multiplexed Gratings	45.9%	±1.0°
Only Large Bandgap	45.6%	–
Only Small Bandgap	36.7%	–

Table 4.1: Optimized efficiency and angular spans of dispersed outputs for each type of spectrum splitter compared to an ideal splitter and to single bandgap systems.

the efficiency performance of e.g. dichroic filters, these holographic elements have the advantage of decoupling diffracted wavelengths and angles thus providing more flexibility in the engineering of such systems. Further, holographic elements have the potential to include features for solar concentration although this aspect was not considered here.

Finally, in this work we paid particular attention to the dispersion performance of these systems because of the direct effect that dispersion has on the positioning of PV cells within a system and the size—and therefore cost—of the PV cells. The addition of a second grating in the multi-grating spectrum splitters we explored clearly improves dispersion performance over a similar single-grating splitter. Going beyond two gratings can reduce overall dispersion further but at the expense of lower system efficiency due to additional spurious diffraction orders. This is especially true in multiplexed-grating systems.

Chapter 5

Multi-grating Systems for Spectral Beam Combining

Introduced in Section 1.2, spectral beam combining (SBC) systems are used to generate high laser radiance from several lower radiance sources. The input sources each operate at a different wavelength, and therefore, the higher power at the output comes at the expense of a wider output bandwidth. A goal of many SBC systems is to increase the output radiance in a manner that minimizes growth in output bandwidth. Equivalently, the goal is to increase the number of input channels operating within a fixed bandwidth which may be limited by the gain bandwidth of a particular type of laser. Channel density cannot be increased without limit, of course, due primarily to crosstalk effects among channels. In this chapter we compare the relative merits and limitations of sequential-grating and multiplexed-grating systems based on transmission-mode volume Bragg gratings (VBGs). We first explore the differing design constraints and loss mechanisms

between these system types. Then in Section 5.2, we introduce an optimization heuristic that reveals regions of the design space which provide the highest channel densities for plane-wave and finite-beam inputs.

5.1 Volume Gratings in SBC Systems

We explored three classes of spectral beam combining systems based on volume Bragg gratings. The first two utilize gratings in sequential arrangements. The sandwiched arrangement is analogous to the sandwiched solar spectrum splitters from Section 4.1.1. The cascaded arrangement is similar to the sandwiched arrangement but with spacing between the individual HOEs. The third class of system utilizes a single HOE comprised of multiplexed gratings in a similar fashion to the multiplexed-grating solar spectrum splitters from Section 4.1.2.

The first type of sequential grating system we have termed a cascaded system. A notional schematic of a three-channel cascaded-grating system is shown in Fig. 5.1. In this system, inputs A, B, and C operate at different wavelengths and are combined into the output D. At each stage, a separate HOE is used to add the input channel to the intermediate beam. In the ideal case, Input A passes through both gratings unchanged, Input B is diffracted by the first grating with 100% efficiency and passes through the second grating unchanged, and Input C is diffracted by the second grating without loss.

It is notable that while Fig. 5.1 depicts a transmission-mode system, and we only consider transmission-mode systems here, many sequential systems utilize reflection-mode gratings to achieve a nearly flat passband in terms of angular

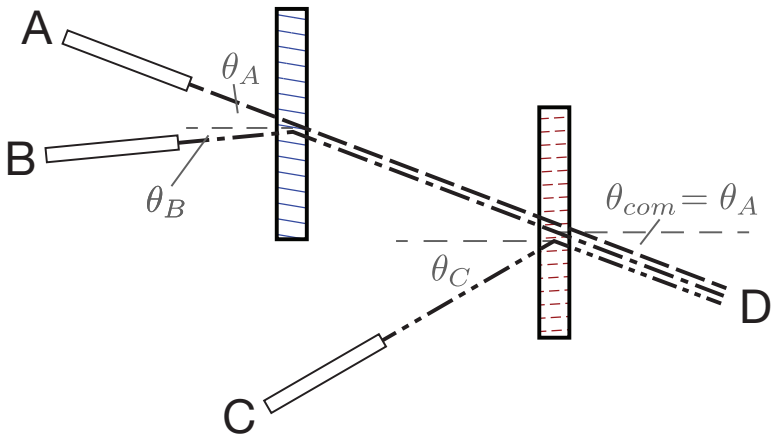

Figure 5.1: Schematic of a three-channel transmission-mode cascaded-grating SBC system utilizing two single-grating HOEs. Inputs A, B, and C operate at different wavelengths and enter the system at angles θ_A, θ_B, and θ_C respectively. These inputs are combined into the output D which leaves the system at angle $\theta_{com} = \theta_A$.

detuning from the Bragg condition (see e.g. [46]). This improves performance when non-plane-wave inputs are used. We explore finite beam inputs further in Section 5.2.2.

A disadvantage of the cascaded arrangement is the physical size required to allow input beams to enter the system between the HOEs. If we eliminate this space, we arrive at the sandwiched-grating arrangement depicted in Fig. 5.2. Again, in the ideal case, a particular input would be diffracted strongly by one grating and unaffected by the other gratings. The exception is, of course, Input A—the "through-beam"—which is ideally not affected by any grating. In contrast to the cascaded arrangement, though, here all inputs pass through all of the HOEs increasing opportunities for loss due to spurious diffraction in the non-ideal case.

Finally, the multiplexed-grating system is shown in Fig. 5.3. Here each of the sinusoidal index of refraction patterns typical of volume phase gratings are present

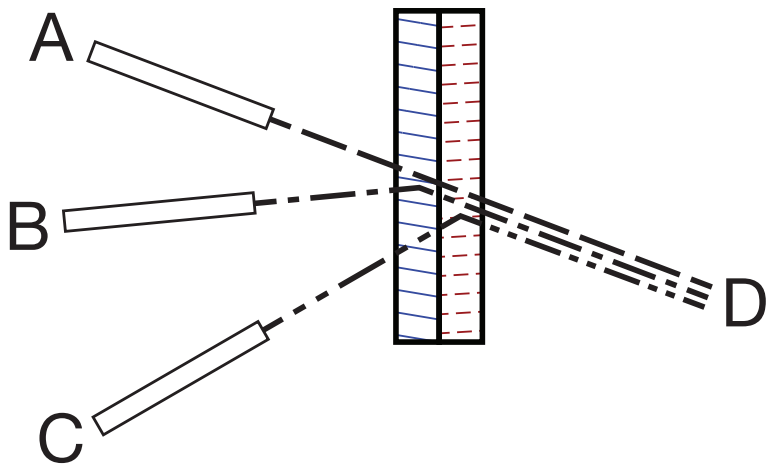

Figure 5.2: Schematic of a three-channel transmission-mode sandwiched-grating SBC system utilizing two single-grating HOEs. Inputs A, B, and C operate at different wavelengths and are combined into the output D. Ideally, Input A is not diffracted by either grating, Input B is strongly diffracted by the first grating and not diffracted by the second, and Input C is strongly diffracted by the second grating and not diffracted by the first.

simultaneously in the same HOE.

5.1.1 Single VBG System

The simplest case of an SBC system based on volume Bragg gratings is a two-channel system utilizing one grating. This is, in fact, a degenerate case of the three system classes previously introduced. If we assume plane-wave inputs linearly polarized perpendicular to the plane of incidence, the diffraction efficiency of the single grating as a function of wavelength can be calculated using Kogelnik's well-known coupled-wave method [1]. This appears as shown in Fig. 5.4 for the two channels' input angles where we assume a material thickness of $d = 0.5$mm, a common output angle for the system of $\theta_{com} = \theta_A = 0°$, an input angle for Input

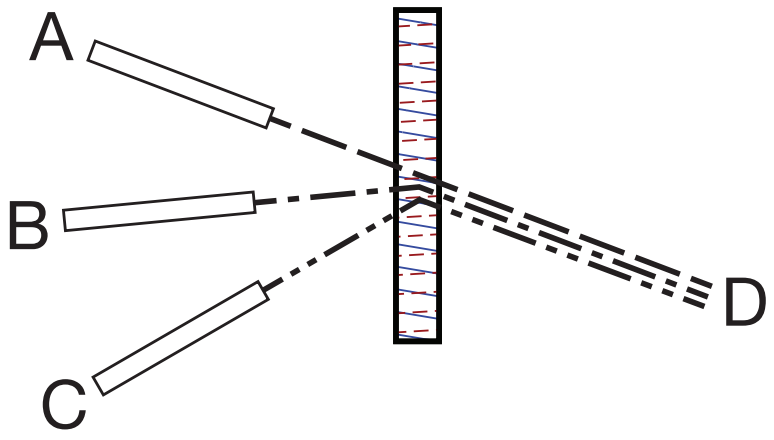

Figure 5.3: Schematic of an ideal three-channel transmission-mode multiplexed-grating SBC system utilizing a dual-grating HOE. Inputs A, B, and C operate at different wavelengths and are combined into the output D. Ideally, Input A is not diffracted by either grating, and inputs B and C are each strongly diffracted by one of the multiplexed gratings but not the other.

B of $\theta_B = 40°$, and an index modulation for the grating such that 100% diffraction efficiency is achieved for Input B.

Conceptually, to achieve 100% efficiency for the single-grating, two-channel system with plane-wave inputs, one simply sets the wavelength for Input A, λ_A, to one of the zeros of the diffraction efficiency curve when calculated for an input angle of θ_A (e.g. $\lambda_A \approx 1039$nm). In this manner, the minimum output bandwidth achievable in this two-channel system is dependent on the parameters that define the grating. In general, though, it is well known that increasing the thickness of the grating or utilizing steeper input and output angles—here, making the output angle more negative—will increase the spectral selectivity of the grating, reducing the spacing between the first zeros and minimizing the output bandwidth of this system.

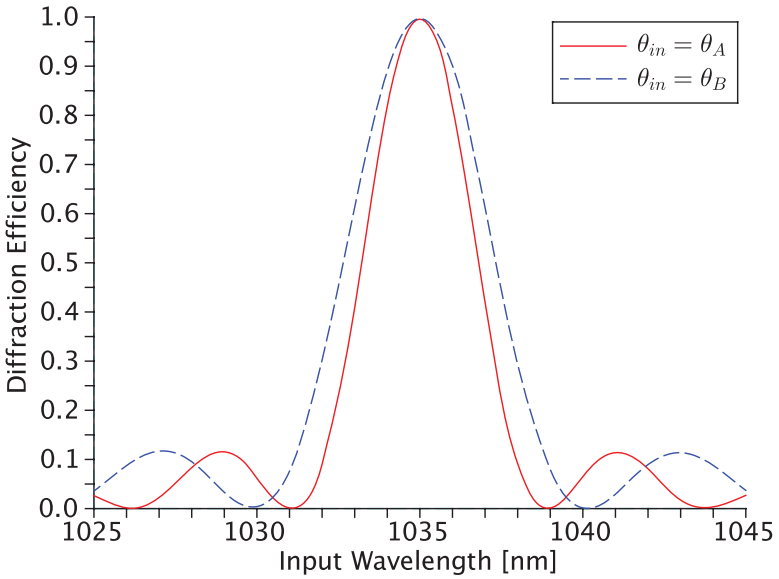

Figure 5.4: Diffraction efficiency of a single volume Bragg grating as a function of wavelength for input angles corresponding to the two channels combined by this HOE. The grating parameters are described in the main text. Note how the horizontal scaling of the diffraction efficiency curve varies depending on which input angle is used.

We can also conceive of a single-grating multichannel system that takes advantage of the dispersion from a single volume grating in much the same way as a surface-relief grating can be applied to spectral beam combining (see Section 1.2). However, this architecture suffers from the same tight coupling between source position and wavelength that the surface-relief grating systems do. Also, at most one input could be Bragg-matched with the grating, and diffraction efficiency could fall off quickly for for the other inputs. This limits the overall combining efficiency of such a system especially for those using a transmission-mode grating. This type of system is not considered further here.

5.1.2 Sequential-grating Systems

When one goes beyond a single grating in the system, it becomes increasingly difficult to align diffraction efficiency peaks and zeros. The end result is a system that exhibits unwanted loss due to spurious diffraction. Following inputs A and B through such a system by referring to Fig. 5.5, the first grating (denoted G1) exhibits 100% diffraction efficiency for an input ($\lambda_B = 1035\text{nm}, \theta_B$), and the second grating (denoted G2) exhibits essentially 0% diffraction efficiency for an input (λ_B, θ_{com}). We therefore can expect Input B to traverse the system without loss. However there is no wavelength for which both gratings exhibit 0% diffraction efficiency for Input A incident at $\theta_A = \theta_{com}$, so we expect some loss for that channel. ($\lambda_A = 1026\text{nm}$ would provide close to ideal performance.)

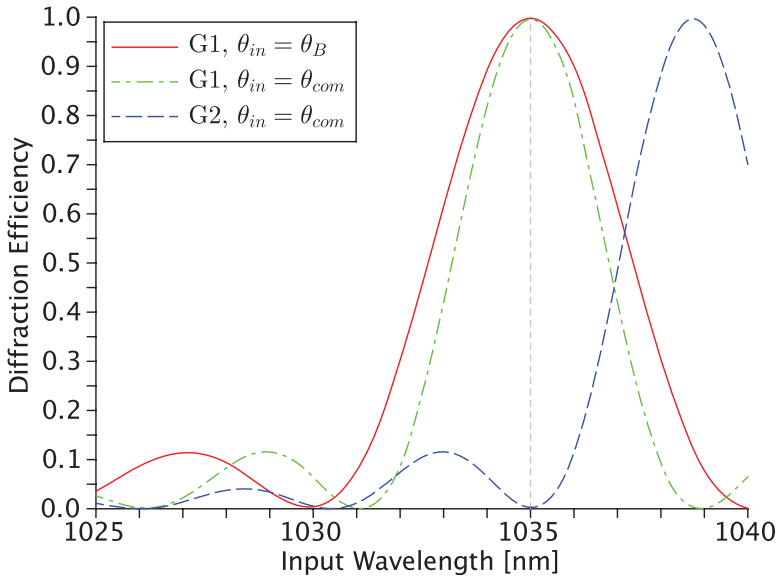

Figure 5.5: Diffraction efficiency curves vs. wavelength for two gratings, G1 and G2, in a sequential-grating SBC system for the input angles corresponding to Inputs A and B.

Again referring to Fig. 5.5, Input C in a cascaded arrangement (see Fig. 5.1) would only interact with the second grating, so 100% diffraction efficiency could be expected. However, for no loss in a sandwiched arrangement (Fig. 5.2), there would need to be an operating point (λ_C, θ_C) where the diffraction efficiency of grating 1 is 0% while the diffraction efficiency of grating 2 is 100%. Inputs B and C necessarily enter the system at different angles (i.e. $\theta_B \neq \theta_C$), so low-loss for both channels could be relatively easily achieved at the second grating. However, one can see how the general conditions of low loss, multiple gratings, and narrow, fixed bandwidth are quite difficult to achieve simultaneously.

5.1.3 Multiplexed-grating Systems

The loss mechanisms for a multiplexed-grating arrangement are more complex still. When more than one grating is present in a single HOE, one can no longer merely attempt to align appropriate peaks and zeros in the various individual diffraction efficiency curves. Rather, the gratings must be treated simultaneously for an input at a particular wavelength and angle, and this forces changes to the set of coupled-wave equations describing the interaction. (The algorithmic matrix method developed in Chapter 2 is employed in Section 5.2 when calculating diffraction efficiencies and other characteristics of these multiplexed-grating arrangements.)

In a sandwiched- or cascaded-grating arrangement, the system of two gratings explored in Fig. 5.5 was expected to provide near 100% system efficiency for its three inputs. If we collapse those two gratings into a single HOE to create a

multiplexed-grating arrangement, though, the resulting calculated efficiency values are significantly different as shown in Fig. 5.6. Here both Input B and Input C are subject to efficiency losses greater than 10% at their respective wavelengths due to spurious waves and grating cross-coupling occurring within the single HOE.

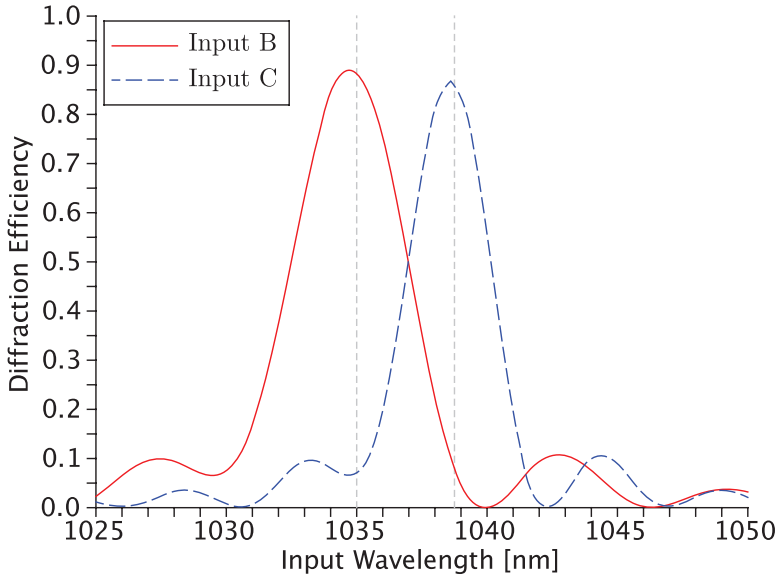

Figure 5.6: Diffraction efficiencies at the system output for inputs B and C of a two-grating multiplexed SBC system formed by trivially collapsing the two gratings of a sandwiched-grating system into a into a single HOE.

Some insight can be gained by investigating the diffraction efficiency for Input B as a function of depth, z, in the grating as shown in Fig. 5.7. This essentially depicts the transfer of energy between the given input wave and desired output wave as these waves travel through the HOE from $z = 0$ to $z = d$ where d is the thickness of the material. One curve in the figure represents this energy transfer for an HOE with only Grating 1 present, and we can see that the curve reaches 100% energy transfer at $z = d$ as desired. The other curve, though, represents this energy transfer with Grating 2 present in the HOE as well, and we can see that

not only does the energy transfer peak occur for $z \neq d$, but, more importantly, the curve never reaches 100% energy transfer. In general some of the energy that is not transferred into the output wave of interest remains in the input wave and some is diffracted into a spurious wave.

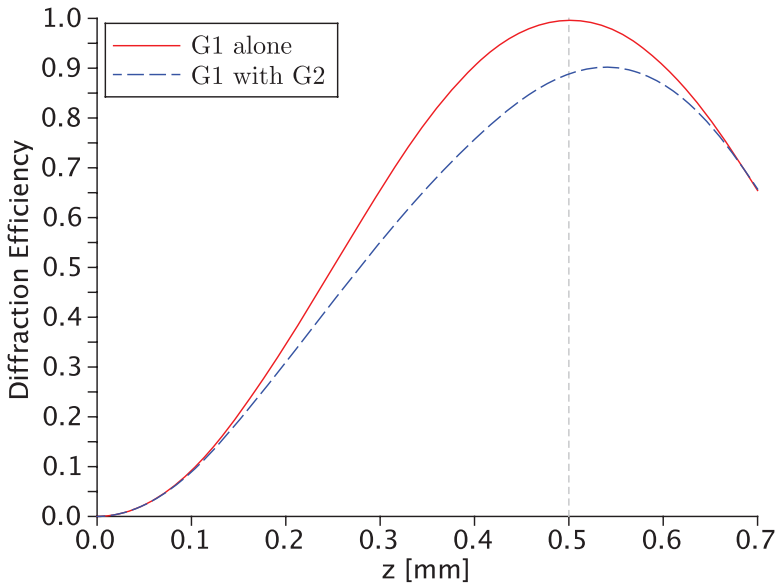

Figure 5.7: Diffraction efficiency of Grating 1 as a function of HOE depth, z, for Input B satisfying the Bragg condition. One curve shows the efficiency with Grating 1 alone (i.e. Grating 2 is not present in the HOE). The other curve shows the effect of adding Grating 2 to the HOE. The vertical dashed line indicates $z = d$ where d is the thickness of the HOE.)

Clearly it is non-trivial to design an SBC system especially as the number of channels increases. Given physical constraints (overall size, input angles, etc.) on a sequential-grating system, it is not practical in general to achieve perfect alignment of all pertinent combinations of diffraction efficiency peaks and zeros for all gratings. Multiplexed-grating systems, despite the advantages that come with having a single HOE, further suffer from inter-grating interference effects

within that single HOE.

For some applications, it has been correctly suggested that cross-coupling and inter-grating interference effects can be essentially eliminated through wide separation of channel wavelengths [36, 37]. This, however, is counter to our goal of maximizing channel density in an SBC system given a fixed operating bandwidth.

In the next section we introduce a optimization method that aims to find design parameters for SBC systems which provide the highest overall efficiency for a fixed system bandwidth given the number of channels in the system. Using this method we compare the relative channel density limits of the different classes of SBC systems. We further explore the effects of non-plane-wave inputs on system performance.

5.2 SBC System Optimization

Optimizing a multi-grating spectral beam combining system is a non-linear problem of many dimensions. In order to explore the solution spaces for multiplexed- and sequential-grating systems, we again employ particle swarm optimization (PSO) as in Section 4.2 to determine a set of parameters that results in the SBC system with the highest overall efficiency given a set of practical constraints.

We define three system-wide variables that are held constant for a given optimization run: the number of channels, N, the material thickness, d, and the common output angle, θ_{com}. Further, the optimizer adjusts three grating variables for each channel: center wavelength (λ_{center}), input angle (θ_{in}), and index modulation, n_1. To compare the effects of different values of the system-wide variables, we

	d [μm]	θ_{com}
Group 1	500	0°
Group 2	500	−30°
Group 3	1000	0°
Group 4	1000	−30°

Table 5.1: System-wide variable constraints placed on the optimization algorithm for each of the four simulation groups.

optimized cascaded-, sandwiched-, and multiplexed-grating SBC systems in the four groups summarized in Table 5.1. For all four groups, we keep the operating bandwidth of the system fixed at 1030–1040nm.

Within each of the four groups, we explored several values of N. In each case, the optimizer adjusts $3N$ parameters (i.e. three grating variables times N channels) which are allowed to vary over the ranges summarized in Table 5.2. Early experiments with this method revealed that the optimizer tended to space channels equally within the given fixed operating bandwidth. To improve the efficiency of the algorithm, we then modified it to assume small adjustments to channel wavelengths around this equal spacing. This eliminates large volumes of the $3N$-dimensional search space where results are known to be quite poor. Likewise, the index modulation for each grating is allowed to vary over a narrow range around the value that would give the grating 100% efficiency in Kogelnik's calculation for a single lossless transmission grating.

The particle swarm is initialized with 200 particles uniformly distributed within the search space with zero velocity. On each iteration, each particle's metric, Ω, is calculated based on the represented SBC system's total diffraction efficiency (i.e.

λ_{center}	$\pm$1nm variation around evenly spaced channels within fixed bandwidth
θ_{in}	$35° - 50°$
n_1	Kogelnik result $\pm 5 \times 10^{-5}$

Table 5.2: Constraints placed on the optimization algorithm for each of the gratings' three independent variables.

the sum of the diffraction efficiencies at each channel's input angle and center wavelength). The best energy for each particle and for the swarm of particles as a whole is tracked, and each particle's new velocity vector, $\boldsymbol{v}_{n+1}$, and new position vector, $\boldsymbol{p}_{n+1}$, are calculated per Eq. 4.6 and Eq. 4.7 respectively. In a similar fashion to the optimization discussed in Section 4.2, values for the simulation variables ω, ϕ_p, and ϕ_g, were again determined through experimentation and are initialized in the optimizer to 0.80, 0.30, and 0.05 respectively. Here, the optimizer runs for 200 iterations, and after 170 iterations these values are changed to 0.55, 0.25, and 0.15 respectively to accelerate convergence to the swarm's best known position. To reinforce the validity of these tuning parameters, we executed the optimizer multiple times under the same constraints and compared the results, expecting the optimizer to return a system with comparable efficiency each time.

The next section explores optimization results for plane-wave inputs. Then the following section explores optimization results when inputs of finite transverse extent are taken into account.

5.2.1 Results for Plane Wave Inputs

In the following subsections we present system efficiency results for optimized multiplexed- and sequential-grating SBC systems operating between 1030nm and 1040nm for increasing numbers of channels. Note that in these simulations, we do not include the through-channel (e.g. channel A in Fig. 5.1). Rather we only include diffracted channels for which there is an associated grating.

Multiplexed-grating Systems

We executed the optimizer for multiplexed-grating SBC systems for each of the four system parameter groups (Table 5.1) for up to 14 channels and an operating band covering 1030–1040nm. In each case, we repeated the optimization five times to check consistency, and results are plotted in terms of system power in Fig. 5.8. System power for each group increases linearly with the number of channels in the system until inter-grating interference effects begin to compromise system efficiency. Note that as performance falls off for a given group, optimization consistency also decreases. Inter-grating interference in these arrangements strongly limits the achievable system efficiency resulting in many solutions with relatively poor performance. Given the optimizer's finite execution time, the best of the poor solutions is not always discovered.

All four groups perform similarly—and rather well—until four channels are included in the system. At this point the inter-grating interference in Group 1 (i.e. the thinner material and shallower output angle) begins to compromise system performance. The remaining three groups continue to perform well until

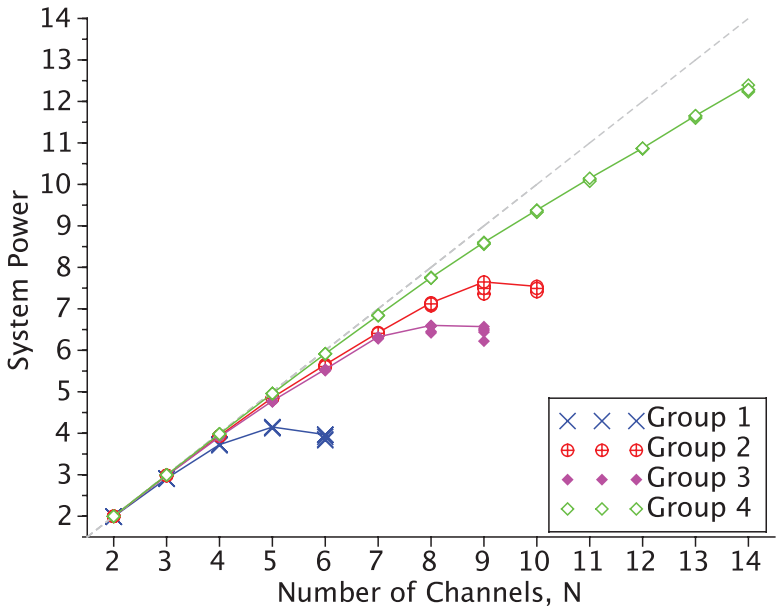

Figure 5.8: Optimized multiplexed-grating system output power for each of the four system parameter groups as a function of the number of channels in the system, N. Operating bandwidth is fixed at 1030–1040nm. Input power per channel is normalized to 1. The diagonal line indicates an ideal system (i.e. 100% efficiency from each channel). Stacked symbols indicate the results of repeated optimizer runs for a given set of inputs.

six channels are employed when the curves for Groups 2 and 3 diverge from the optimal line.

Reviewing the same data in terms of system efficiency rather than system power, it is easier to compare the relative performance of Groups 2 and 3. It is clear from Fig. 5.9 that Group 2 performs slightly better than Group 3 as the number of channels in the system is increased. This suggests that a steeper output angle should be preferred over using a thicker material. And using both a thick material and a steep output angle (i.e. Group 4) exhibits the best performance of all four groups allowing more than 50% more channels than the next best group if we enforce a system efficiency limit of 90%.

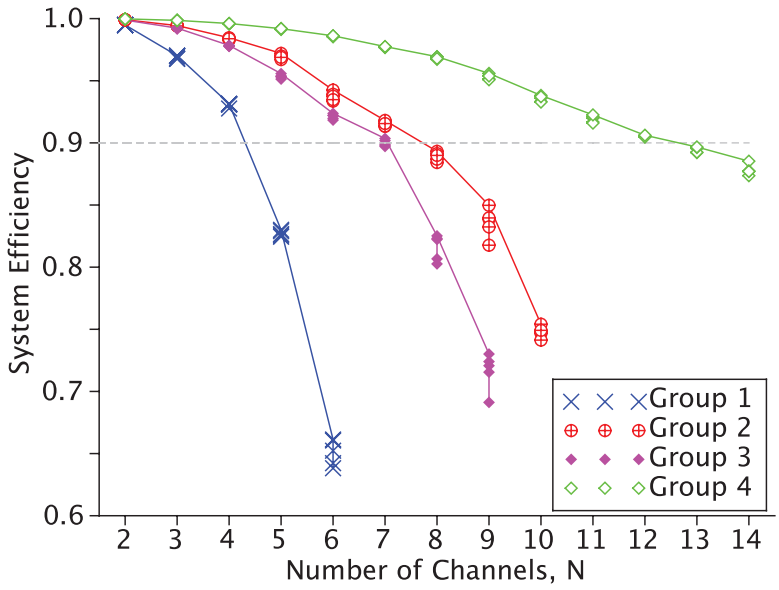

Figure 5.9: Optimized multiplexed-grating system efficiency for each of the four system parameter groups as a function of the number of channels in the system, N. Operating bandwidth is fixed at 1030–1040nm. The dashed horizontal line indicates an arbitrary system efficiency goal of 90%. Stacked symbols indicate the results of repeated optimizer runs for a given set of inputs.

Sequential-grating Systems

As with the multiplexed-grating systems, we also executed the optimizer for cascaded- and sandwiched-grating SBC systems for each of the four groups and for up to 20 channels and an operating band again covering 1030–1040nm. The results for cascaded systems are plotted in terms of system power in Fig. 5.10. Again system power for each group increases linearly with the number of channels in the system until cross-coupling effects begin to compromise system efficiency. In a similar fashion to the multiplexed-grating system, Group 1 is the worst performer, Group 4 the best, and Group 2 slightly outperforms Group 3. This reinforces the notion that steep output angles and thick materials improve channel density, and for the ranges of parameters considered here, a steep output angle improves channel density somewhat more than a thicker holographic material.

The key comparison, though, is the performance of multiplexed-grating systems and sequential-grating systems within the same group. The differing nature of the interference in a sequential system discussed in Section 5.1 allows for many more channels than in a multiplexed-grating system, regardless of group, before system efficiency is compromised. Using 90% system efficiency as a basic metric and referencing Fig. 5.9 and Fig. 5.11, for each of the four groups the cascaded-grating arrangement supports roughly 50% more channels than the multiplexed arrangement in the same group.

Results for sandwiched-grating systems are not plotted here, but as one might expect, these systems outperform multiplexed-grating systems group-by-group, but they do not perform as well as cascaded-grating systems because in the

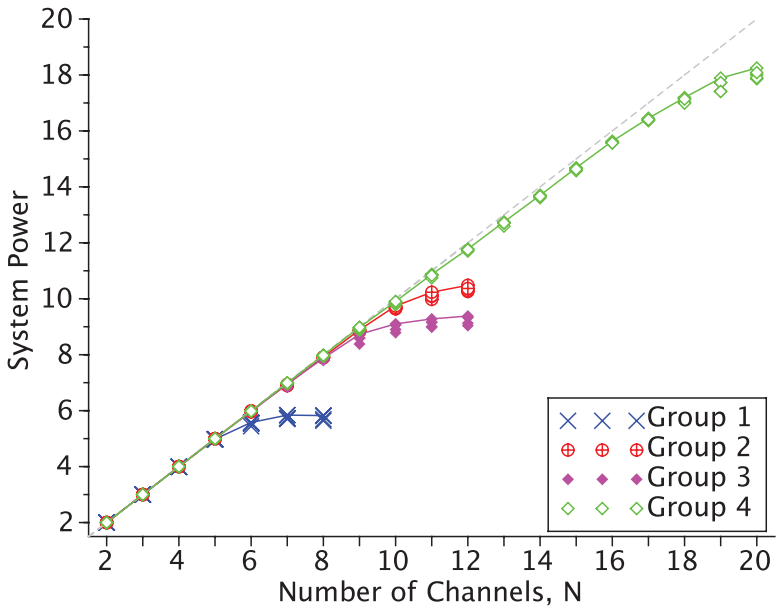

Figure 5.10: Optimized cascaded-grating system output power for each of the four system parameter groups as a function of the number of channels in the system, N. Operating bandwidth is fixed at 1030–1040nm. Input power per channel is normalized to 1. The diagonal line indicates an ideal system (i.e. 100% efficiency from each channel). Stacked symbols indicate the results of repeated optimizer runs for a given set of inputs.

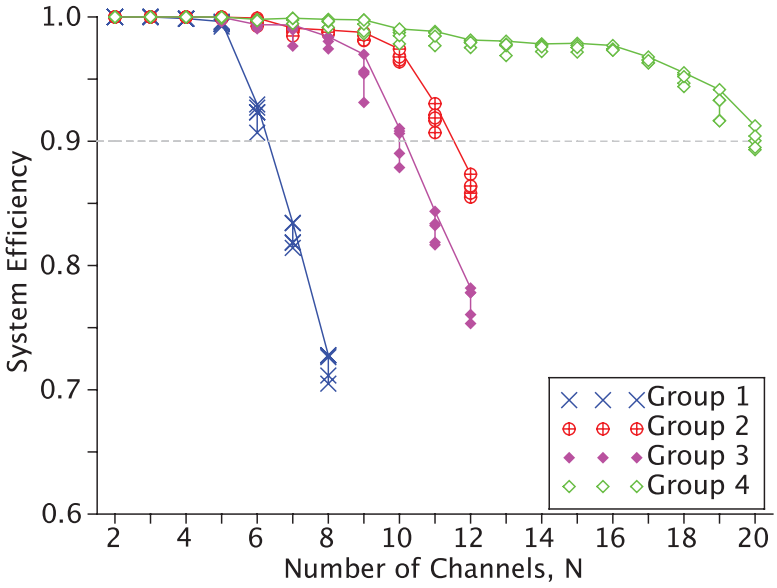

Figure 5.11: Optimized cascaded-grating system efficiency for each of the four system parameter groups as a function of the number of channels in the system, N. Operating bandwidth is fixed at 1030–1040nm. The dashed horizontal line indicates an arbitrary system efficiency goal of 90%. Stacked symbols indicate the results of repeated optimizer runs for a given set of inputs.

sandwiched-grating arrangement, every input must interact with every grating which increases loss. 90% efficiency was achieved for the sandwiched-grating arrangement for 6, 10, 9, and 17 channels for Groups 1–4 respectively.

These results do not suggest, though, that for a practical case a sequential-grating system should always be preferred over a multiplexed-grating system. First, in the optimization calculations, the fixed material thickness is used on a per-grating basis in order to keep the spectral widths of the channels relatively constant. So if an N-channel multiplexed-grating system has a thickness d—with all gratings sharing the same slab of material—an N-channel sandwiched-grating system would have a thickness of Nd with each grating occupying a separate slab of material, and a cascaded-grating system would be larger still because of the spacing between the individual HOEs. If instead we assume that each grating in a sequential system had a thickness of d/N, the spectral widths of the resulting gratings' efficiency curves would be very wide and inter-grating interference would be severe. The multiplexed system would outperform the sequential system in every case.

In addition to the difference in the overall system thickness, other practical considerations need to be made when choosing between a sequential arrangement and a multiplexed one. These include ease and repeatability of assembly, alignment, and thermal management. Depending on these other factors, a multiplexed-grating architecture may be preferred in some cases despite lower efficiency for a given number of channels. However, these considerations must also be weighed against limitations to the number of gratings that can be successfully multiplexed given the dynamic range of the holographic medium and difficulties arising from

multiple exposures (e.g. partial erasure) [47].

5.2.2 Results for Finite Beam Inputs

An important factor that is not considered in the results of the previous section is the angular acceptance of the constituent volume Bragg gratings in these types of SBC systems (i.e. how diffraction efficiency decreases for inputs mismatched in angle from the Bragg condition). Until now only plane wave inputs have been considered in the system optimization algorithm, and as we have shown, parameter groups involving steeper output angles and thicker materials exhibit higher efficiency at higher channel counts. It is clear that favoring these parameters improves channel density because the spectral width of a grating's diffraction efficiency curve narrows as steeper angles and thicker materials are used. This reduction in spectral width for a given grating correlates with a reduction in the effects of inter-grating interference for a given number of channels and a fixed operating spectrum. However, similar narrowing is evident in the *angular* width of the grating's diffraction efficiency curve. If we assume Gaussian inputs of various radii instead of plane wave inputs, and we consider the angular plane wave spectra of these inputs when calculating the diffraction efficiency for each channel (see e.g. [48]), there must be a compromise between increasing angles and/or thickness to narrow spectral width (i.e. to increase channel density) and decreasing angles and/or thickness to improve angular acceptance (i.e. to reduce per-channel loss due to non-diffracted power).

The relative sizes of the angular acceptance curve of a typical Group 1 grating

and the angular plane wave spectra for various Gaussian beam widths (assuming a wavelength of 1035nm) are depicted in Fig. 5.12. Clearly, even for a beam radius of 1mm, the width of the beam's angular plane wave spectrum is significant relative to the width of the central lobe of the grating's diffraction efficiency curve. This will result in a decrease in per-channel efficiency independent of inter-grating interference effects as depicted in Fig. 5.13.

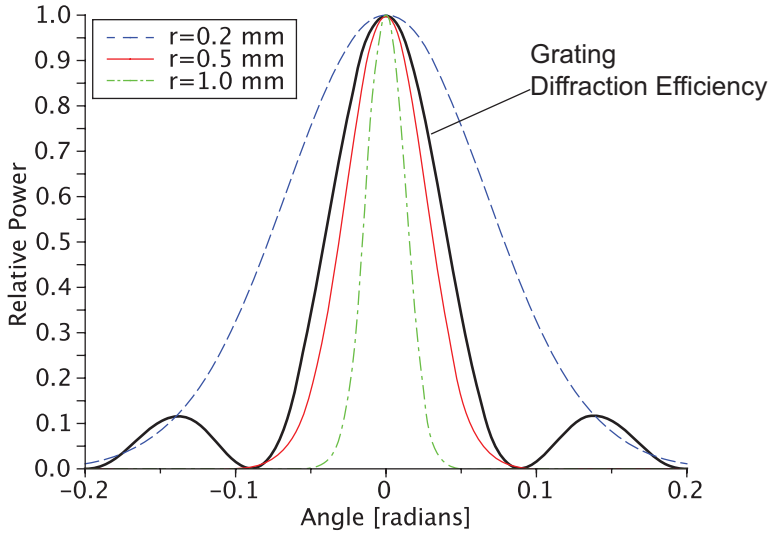

Figure 5.12: Relative angular widths for Gaussian inputs at 1035nm with various radii compared with the diffraction efficiency as a function of input angle (for a fixed wavelength) of a typical Group 1 grating centered at 1035nm.

The following sections present optimization results for SBC systems accounting for these finite input widths. The optimization algorithm was modified to use the beam radius as an additional system-wide variable. Diffraction efficiencies at 15 angles between the $1/e^2$ points of the Gaussian angular plane wave power spectrum are weighted, calculated, and combined to give an aggregate diffraction efficiency for that channel given the beam radius. (Beam shape and beam quality are not

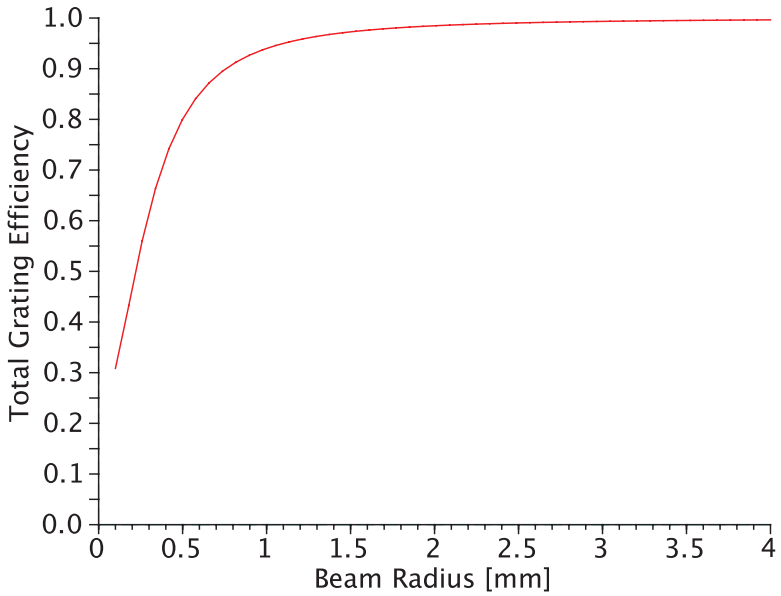

Figure 5.13: Total efficiency for a single, Group 1 grating designed for 1035nm as a function of input beam radius.

considered here.)

Output Angle Optimization

We begin by keeping the thickness of the holographic material fixed at 0.5mm and allowing the optimizer to vary the channels' common output angles between 0 and -30 degrees. That is, in addition to selecting center wavelengths, modulation levels, and input angles for each channel, the optimizer is also choosing a common output angle for the system between the angles previously defined for Groups 1 and 2.

The system efficiency results as a function of beam radius for this exercise are shown in Fig. 5.14 for a five-channel multiplexed-grating system. Also depicted for comparison are the optimization results if the system output angle is kept fixed

at 0° (Group 1) and −30° (Group 2).

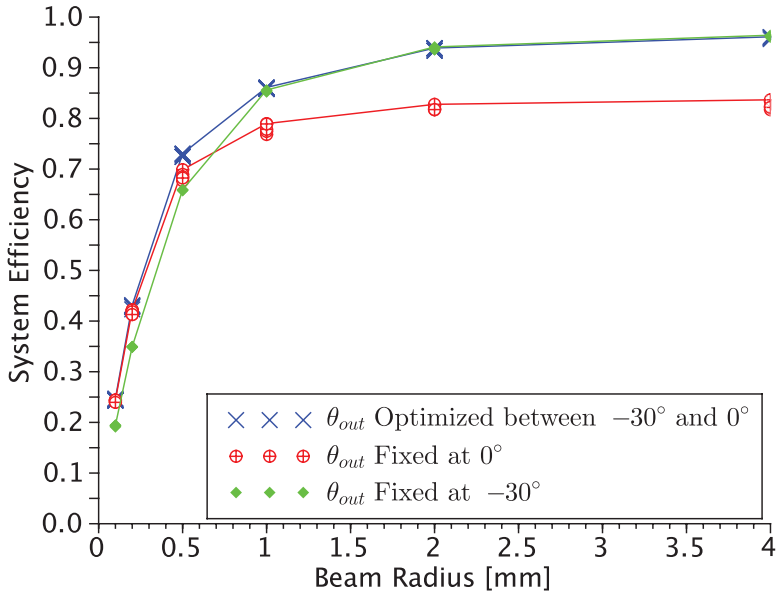

Figure 5.14: Efficiency of a five-channel multiplexed-grating system as a function of input beam radius. The material thickness is kept constant at 0.5mm. The three curves indicate the efficiency results with the system output angle fixed at 0° (Group 1), fixed at −30° (Group 2), and optimized between those two angles. Stacked symbols indicate the results of repeated optimizer runs.

For a large beam radius, the angle-optimized system performs as well as the Group 2 system. This is because for large beam radius, the system is not constrained by angular clipping, and the optimizer simply selects the steepest allowed output angle (−30° in this case) to minimize inter-grating interference. However, as the beam radius decreases, the efficiency of the Group 2 system falls off more quickly that the other systems due to clipping of the inputs' angular plane wave spectra.

At a radius of 0.5mm, the angle-optimized system exhibits the highest-efficiency because it uses an output angle that is a compromise between angular clipping

and inter-grating interference. For this input radius, the steeper $-30°$ output angle gives rise to clipping of the angular spectra of the inputs while the shallower $0°$ output angle results in a system that is limited by inter-grating interference.

For radii less than 0.5mm the effect of angular clipping supersedes the effect of inter-grating interference and the performance of the angle-optimized system converges with the Group 1 system. That is, the optimizer selects the shallowest-available angle to minimize per-channel loss due to angular clipping despite the inter-grating interference that is also present.

The output angles selected by the optimizer are plotted versus input beam radius in Fig. 5.15. The trend of the optimizer selecting a shallower common output angle for small beam radii is clear. Note though, the relative inconsistency of the selected output angle for small radii shown in Fig. 5.15 despite the consistency in the system efficiency from the same optimization runs shown in Fig. 5.14. This suggests that as the best-attainable system efficiency—the parameter that the algorithm is optimizing—decreases, there are many combinations of system parameters that can achieve that efficiency as angular clipping is traded against inter-grating interference.

Similar data for output angle optimization in both a cascaded- and sandwiched-grating system was generated but is not included here. The trends are similar to the multiplexed-grating system. For large input beam radii, the optimizer tends toward the steepest output angle available to minimize cross-coupling among the gratings. As the input beam radius decreases, the optimizer decreases the common output angle of the system to reduce clipping of the input beams despite increasing cross-coupling.

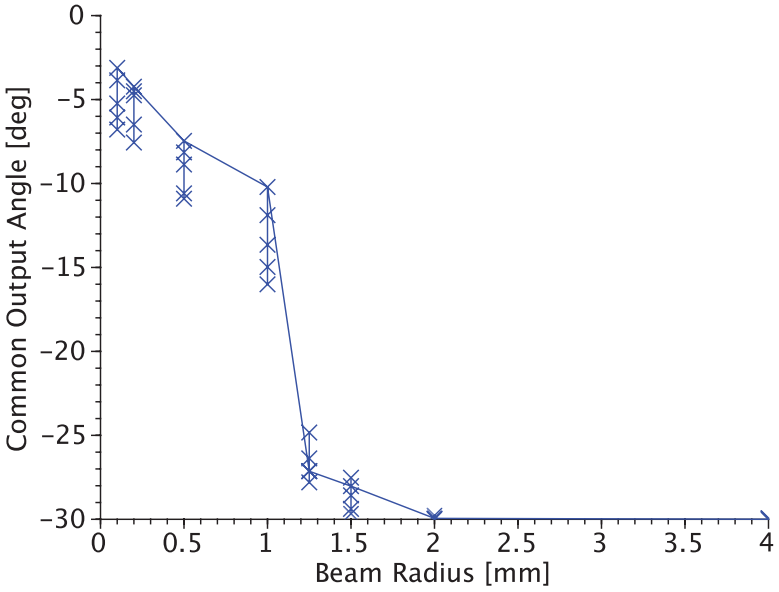

Figure 5.15: Optimized output angle for a five-channel multiplexed-grating system as a function of input beam radius. The material thickness is kept constant at 0.5mm. Stacked symbols indicate the results of repeated optimizer runs, and the solid line indicates the angles associated with the highest achieved system efficiency (see Fig. 5.14) for a given input beam radius.

Again, of course, the overall efficiency of these sequential arrangements decreases dramatically as the input beam radius drops below approximately 1mm just like the multiplexed-grating arrangement. Given the constraints of a particular group and a fixed operating bandwidth, there is a beam radius below which angular clipping effects dominate resulting in poor performance regardless of whether the SBC system uses multiplexed or sequential gratings.

Output Angle and Thickness Limitations

In the previous section, we used our PSO algorithm to select an optimum output angle for an SBC system in addition to optimizing the parameters for each diffracted channel. This was performed for a range of beam radii but for a fixed thickness. In this section we show optimization results for multiplexed-grating SBC systems over variation in hologram thickness as well. Again for each case the optimization algorithm arrives at the best common output angle for the system given other parameters although the final output angles are not shown here.

Figure 5.16 shows regions of the holographic element thickness (d) versus beam radius (r) space for which $\geq 90\%$ system efficiency can be achieved in a multiplexed-grating system for a given number of channels. In the upper-right of the plot (i.e. for inputs approaching plane waves and for thicker materials), the highest numbers of channels are supported. With (near) plane wave inputs, the systems are not limited by angular clipping, so the optimizer is free to choose the steepest available output angle (-30°), and the results approach the Group 4 results shown in Fig. 5.9. That is, for $r = \infty$—or, in fact, $r \geq 4.00$mm for the systems described—and $d = 1.00$mm a multiplexed-grating system can support

$N \leq 12$ with at least 90% efficiency, or $N_{max} = 12$. (Note that the plot only shows up to $N = 7$ for clarity.)

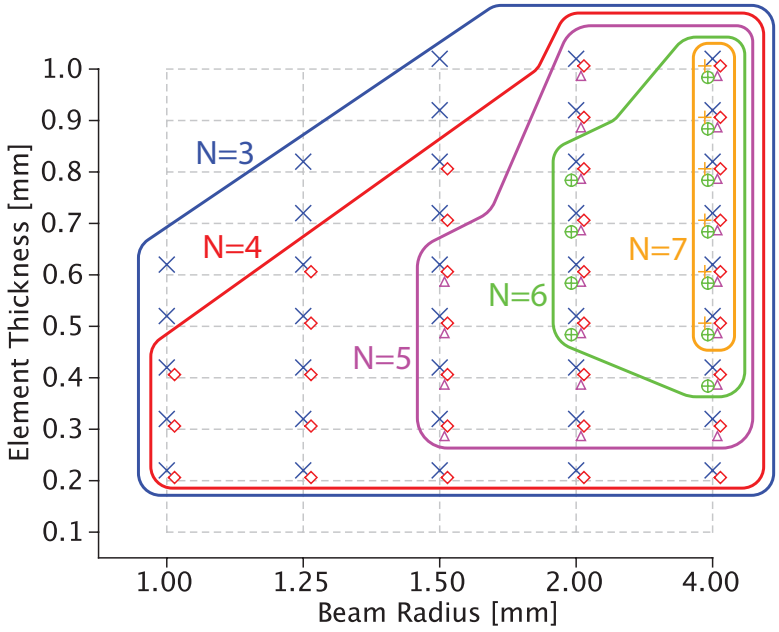

Figure 5.16: Regions of beam radius (r) and holographic element thickness (d) where 90% system efficiency can be achieved in a multiplexed-grating architecture for various numbers of channels, N. The PSO optimizer was executed for combinations of thickness and radius at the intersections of the dashed lines, and the mark representing a particular number of channels is included at an intersection if the optimized system efficiency exceeded 90%.

Continuing clockwise to the lower-right region of Fig. 5.16, we can see the effects of inter-grating interference on overall system efficiency. As the thickness of the material decreases to 0.5mm, the optimizer again favors a steeper common output angle, and the results match the Group 2 results in Fig. 5.9 for plane wave inputs ($N_{max} = 7$). The optimizer is not allowed to increase the common output angle beyond $-30°$, so as the hologram thickness decreases below 0.5mm, N_{max} decreases due to inter-grating interference.

Moving to the lower-left region of Fig. 5.16, there is not a significant difference in N_{max} as the beam radius decreases. In this region, the material is relatively thin and the optimizer can additionally reduce the common output angle, both of which tend to avoid loss due to angular clipping which is typically present for lower values of r. However, a thin material and a shallow output angle together lead to significant inter-grating interference (cf. Group 1 in Fig. 5.9), so the number of supported channels, N_{max}, remains small.

Finally, inspecting the upper-left region of Fig. 5.16, we note that the multiplexed-grating system cannot support even a small number of diffracted channels when utilizing thicker materials and smaller beam radii. $N_{max} \to 0$ simply due to angular clipping.

For sequential-grating systems, the numbers of supported channels under a 90%-efficiency constraint follow Fig. 5.11 for cascaded-grating systems as $r \to \infty$. Also, N_{max} falls off quite similarly to the trends shown in Fig. 5.16 as $r \to 0$ because, again, power loss due to angular clipping affects both sequential- and multiplexed-grating SBC systems in an essentially equivalent manner.

5.3 Conclusion

Spectral beam combining systems utilizing multiple volume Bragg gratings must be carefully analyzed to maximize performance. This analysis grows increasingly difficult as the number of channels—and therefore the number of variables—increases, and heuristic optimization techniques are useful tools for exploring the limits of these systems.

Of the three system classes discussed, the highest channel densities were achieved by cascaded-grating systems because each input beam in such a system only interacts with subsequent gratings in the cascade. However, this also leads to cascaded-grating systems being physically larger than the other two classes due to the required spaces between the single-grating HOEs.

Sandwiched-grating systems exhibited the next best channel densities, only slightly lower than cascaded-grating systems. This decrease is due to each input beam interacting with all of the individual gratings in the system but comes with the advantage of a more compact arrangement.

The multiplexed-grating system exhibited the poorest performance of the three system classes. It is also the most difficult to analyze being subject to inter-grating interference effects within its single HOE. Requiring only one HOE, though, is a distinct advantage to this type of system.

Finally, when non-plane-wave inputs are used with any of these grating arrangements, overall system efficiency drops quickly as beam radii decrease. This is due to limited angular acceptance in these volume Bragg gratings which affects all three arrangements roughly equally. However, when used in high-power spectral beam combining applications, these volume gratings would most likely be designed for use with expanded beams to account for thermal limitations, and less attention would need to be paid to beam radius considerations.

Chapter 6

Conclusions

The work of the preceding chapters has shown that volume Bragg gratings are useful elements when working with spectral systems. While using a single VBG in a spectral system can be relatively straightforward, employment of multiple VBGs can improve performance but results in complicated interactions among the gratings that must be carefully analyzed. This is true in cascaded and sandwiched sequential-grating systems, and these grating interactions become more complex in multiplexed-gratings systems. Regardless of the system architecture, the mathematical method developed in Chapter 2 and verified experimentally in Chapter 3 is a valuable tool for engineering and optimizing these multi-grating systems.

As the heuristic optimization results from Chapter 4 and Chapter 5 showed, sequential grating systems tend to outperform similar multiplexed grating systems for both solar spectrum splitters and spectral beam combiners. The effects of inter-grating interference are more impactful to multiplexed-grating systems. Despite

this loss of system efficiency, though, and despite the increased computational complexity for analysis, multiplexed-grating systems still have the advantage of requiring only a single HOE.

Both cascaded-grating and sequential-grating arrangements were considered for spectral beam combining systems. (The cascaded arrangement as described in Chapter 5 would not be practical for solar spectrum splitters as the sun provides the only input.) These arrangements showed similar performance with the cascaded-grating systems exhibiting better overall efficiency. This is because a given input channel needs to pass through only subsequent gratings in the cascade and is thus subject to fewer opportunities for cross-coupling. In a sandwiched grating system, all input channels must pass through all HOEs, but the reduced efficiency is a tradeoff weighed against the mechanical compactness of the sandwiched arrangement. As with any engineering problem, there are tradeoffs among the multi-grating architectures considered here related to efficiency, size, compactness, ease of assembly and alignment, etc.

There are several areas where the work presented here can be extended. First, both solar spectrum splitting and spectral beam combining applications using reflection-mode gratings were not explored in detail. While there are mechanical advantages to transmission geometries, we expect that the nearly flat passband that is characteristic of reflection-mode volume Bragg gratings could be advantageous to both spectral splitting and beam combining. In the former, the flat passbands and steep transitions as a function of wavelength could provide a more efficient spectral filter overall. In the latter case, the flat passband characteristic as a function of incident angle could improve system efficiency for finite-beam

inputs. However in both cases, the systems must be analyzed in detail to determine the exact nature of the inter-grating interference that limits performance in these systems. An extension to the mathematical model from Chapter 2 to support reflection gratings—as well as multiplexed combinations of transmission and reflection gratings—is included in Appendix B.

Another area that may prove fruitful for future work is polarization multiplexing. That is, increasing the channel density of spectral beam combining systems by exploiting orthogonal polarizations. The work presented in Chapter 5 assumed that inputs are polarized perpendicular to the plane of incidence with the grating. However, for in-plane polarization, Eq. 2.21 indicates that if the polarization of the input wave and diffracted wave differ by 90°, the effective coupling coefficient, and therefore the diffraction efficiency of the grating, goes to zero. One could take advantage of this to potentially reuse channel wavelengths in orthogonal polarizations thus doubling the number of channels in an SBC system without significant efficiency loss and without increasing the output bandwidth. A set of inputs could be combined by one HOE in such a way that the combined output can pass through a second similar (or potentially identical) HOE with low loss. The two HOEs would be arranged in a cascade such that their outputs are collinear.

Bibliography

[1] H. Kogelnik, "Coupled Wave Theory for Thick Hologram Gratings," Bell Syst. Tech. J. **48**, 2909–2947 (1969).

[2] R. Alferness, "Analysis of Optical Propagation in Thick Holographic Gratings," Appl. Phys. **7**, 29–33 (1975).

[3] R. Alferness and S. K. Case, "Coupling in Doubly Exposed, Thick Holographic Gratings," J. Opt. Soc. Am. **65**, 730–739 (1975).

[4] S. K. Case, "Coupled-Wave Theory for Multiply Exposed Thick Holographic Gratings," J. Opt. Soc. Am. **65**, 724–729 (1975).

[5] K. Tu, T. Tamir, and H. Lee, "Multiple-scattering theory of wave diffraction by superposed volume gratings," J. Opt. Soc. Am. A **7**, 1421–1435 (1990).

[6] J. H. Zhao, X. N. Shen, and X. Y. Xia, "Beam splitting, combining, and cross coupling through multiple superimposed volume-index gratings," Opt. Laser Technol. **33**, 23–28 (2001).

[7] R. Kowarschik, "Diffraction efficiency of sequentially stored gratings in transmission volume holograms," Opt. Acta **25**, 67 (1978).

[8] R. Kowarschik, "Diffraction efficiency of sequentially stored gratings in reflection volume holograms," Opt. Quantum Electron. **10**, 171–178 (1978).

[9] V. Minier, A. Kevorkian, and J. M. Xu, "Superimposed Phase Gratings in Planar Optical Wave-guides for demultiplexing applications," IEEE Photon. Technol. Lett. **5**, 330–333 (1993).

[10] V. Minier and J. M. Xu, "Coupled-mode Analysis of Superimposed Phase Grating Guided-wave Structures and Intergrating Coupling Effects," Opt. Eng. **32**, 2054–2063 (1993).

[11] M. G. Moharam and T. K. Gaylord, "Rigorous coupled-wave analysis of planar-grating diffraction," J. Opt. Soc. Am. **71**, 811–818 (1981).

[12] R. R. King, A. Boca, W. Hong, X. Q. Liu, D. Bhusari, D. Larrabee, K. M. Edmondson, D. C. Law, C. M. Fetzer, S. Mesropian, and N. H. Karam, "Band-gap-engineered architectures for high-efficiency multijunction concentrator solar cells," 24th European Photovoltaic Solar Energy Conference, 21-25 September 2009, Hamburg, Germany pp. 55–61 (2009).

[13] A. Barnett, "Very high efficiency solar cell modules," Prog. Photovoltaics Res. Appl. **17**, 75–83 (2009).

[14] X. Wang, N. Waite, P. Murcia, K. Emery, M. Steiner, F. Kiamilev, K. Goossen, C. Honsberg, and A. Barnett, "Lateral spectrum splitting concentrator photovoltaics: direct measurement of component and submodule efficiency," Prog. Photovolt: Res. Appl. **20**, 149–165 (2011).

[15] C. N. Eisler, E. D. Kosten, E. C. Warmann, and H. A. Atwater, "Polyhedral specular reflector design for ultra high spectrum splitting solar module efficiencies (>50%)," Proc. SPIE **8821**, 88210B (2013).

[16] E. D. Kosten, E. C. Warmann, J. Lloyd, and H. A. Atwater, "Spectrum splitting photovoltaics: light trapping filtered concentrator for ultrahigh photovoltaic efficiency," Proc. SPIE **8821**, 882109 (2013).

[17] D. Lin, E. Torrey, J. Leger, and P. Cohen, "Lossless holographic spectrum splitter in lateral photovoltaic devices," in *2011 37th IEEE Photovoltaic Specialists Conference* (IEEE, 2011), pp. 894–898.

[18] D. Zhang, Y. Wu, J. M. Russo, M. Gordon, S. Vorndran, and R. K. Kostuk, "Optical performance of dichroic spectrum-splitting filters," J. Photon. Energy **4**, 043095 (2014).

[19] M. A. Green, *Solar cells: operating principles, technology, and system applications* (Prentice-Hall, 1982).

[20] W. H. Bloss, M. Griesinger, and E. R. Reinhardt, "Dispersive concentrating systems based on transmission phase holograms for solar applications," Applied Optics **21**, 3739 (1982).

[21] D. Zhang, M. Gordon, J. M. Russo, S. Vorndran, and R. K. Kostuk, "Spectrum-splitting photovoltaic system using transmission holographic lenses," J. Photon. Energy **3**, 034597–034597 (2013).

[22] J. M. Castro, D. Zhang, B. Myer, and R. K. Kostuk, "Energy collection efficiency of holographic planar solar concentrators," Applied Optics **49**, 858–870 (2010).

[23] T. Y. Fan, "Laser beam combining for high-power, high-radiance sources," IEEE J. Sel. Topics Quantum Electron. **11**, 567–577 (2005).

[24] E. J. Bochove, "Theory of spectral beam combining of fiber lasers," IEEE J. Quantum Electron. **38**, 432–445 (2002).

[25] S. Klingebiel, F. Roser, B. Ortac, J. Limpert, and A. Tunnermann, "Spectral beam combining of Yb-doped fiber lasers with high efficiency," J. Opt. Soc. Am. B **24**, 1716–1720 (2007).

[26] T. H. Loftus, A. M. Thomas, P. R. Hoffman, M. Norsen, R. Royse, A. Liu, and E. C. Honea, "Spectrally Beam-Combined Fiber Lasers for High-Average-Power Applications," IEEE J. Sel. Topics Quantum Electron. **13**, 487–497 (2007).

[27] P. Madasamy, D. R. Jander, C. D. Brooks, T. H. Loftus, A. M. Thomas, P. Jones, and E. C. Honea, "Dual-grating spectral beam combination of high-power fiber lasers," IEEE J. Sel. Topics Quantum Electron. **15**, 337–343 (2009).

[28] K. Aoyama and J. Minowa, "Optical demultiplexer for a wavelength division multiplexing system," Applied Optics **18**, 1253–1258 (1979).

[29] K. Aoyama and J. Minowa, "Low-loss optical demultiplexer for WDM systems in the 0.8μm wavelength region," Applied Optics **18**, 2834–2836 (1979).

[30] I. V. Ciapurin, L. B. Glebov, L. N. Glebova, V. I. Smirnov, and E. V. Rotari, "Incoherent combining of 100-W Yb-fiber laser beams by PTR Bragg grating," Proc. SPIE **4974**, 209–219 (2003).

[31] B. Chann, A. K. Goyal, T. Y. Fan, A. Sanchez-Rubio, B. L. Volodin, and V. S. Ban, "Efficient, high-brightness wavelength-beam-combined commercial off-the-shelf diode stacks achieved by use of a wavelength-chirped volume Bragg grating," Opt. Lett. **31**, 1253–1255 (2006).

[32] A. Sevian, O. Andrusyak, I. V. Ciapurin, V. I. Smirnov, G. B. Venus, and L. B. Glebov, "Efficient power scaling of laser radiation by spectral beam combining," Opt. Lett. **33**, 384–386 (2008).

[33] P. Boffi, M. C. Ubaldi, D. Piccinin, C. Frascolla, and M. Martinelli, "1550-nm volume holography for optical communication devices," IEEE Photon. Technol. Lett. **12**, 1355–1357 (2000).

[34] S. F. Chen, C. S. Wu, and C. C. Sun, "Design for a high dense wavelength division multiplexer based on volume holographic gratings," Opt. Eng. **43**, 2028–2033 (2004).

[35] S. Datta and S. R. Forrest, "Low through channel loss wavelength multiplexer using multiple transmission volume Bragg gratings," J. Opt. Soc. Am. A **22**, 1624–1629 (2005).

[36] A. Othonos, J. Bismuth, M. Sweeny, A. Kevorkian, and J. M. Xu, "Superimposed grating wavelength division multiplexing in Ge-doped SiO2/Si planar waveguides," Opt. Eng. **37**, 717–720 (1998).

[37] X. Fu, M. Fay, and T. M. Xu, "18 supergrating wavelength-division demultiplexer in a silica planar waveguide," Opt. Lett. **22**, 1627–1629 (1997).

[38] J. W. Goodman, *Introduction to Fourier optics* (McGraw-Hill, New York, 1996), 2nd ed.

[39] T. Rowland, "Orthonormal basis," `http://mathworld.wolfram.com/OrthonormalBasis.html`.

[40] A. Villamarin, J. Atencia, M. V. Collados, and M. Quintanilla, "Characterization of transmission volume holographic gratings recorded in Slavich PFG04 dichromated gelatin plates," Applied Optics **48**, 4348–4353 (2009).

[41] J. M. Russo, D. Zhang, M. Gordon, S. Vorndran, Y. Wu, and R. K. Kostuk, "Spectrum splitting metrics and effect of filter characteristics on photovoltaic system performance," Opt. Express **22**, A528–A541 (2014).

[42] ASTM Standard G173-03, 2012, "Standard Tables for Reference Solar Spectral Irradiances," ASTM International, West Conshohocken, PA (2012).

[43] A. Heifetz, J. T. Shen, S. C. Tseng, G. S. Pati, J. K. Lee, and M. S. Shahriar, "Angular directivity of diffracted wave in Bragg-mismatched readout of volume holographic gratings," Opt. Commun. **280**, 311–316 (2007).

[44] J. Kennedy and R. Eberhart, "Particle swarm optimization," in *Proceedings of IEEE International Conference on Neural Networks* (IEEE, 1995), pp. 1942–1948.

[45] C. Kittel, *Introduction to solid state physics* (Wiley, 1986).

[46] D. R. Drachenberg, O. Andrusyak, G. B. Venus, V. I. Smirnov, J. Lumeau, and L. B. Glebov, "Ultimate efficiency of spectral beam combining by volume Bragg gratings," Applied Optics **52**, 7233 (2013).

[47] D. Brady and D. Psaltis, "Control of volume holograms," J. Opt. Soc. Am. A **9**, 1167–1182 (1992).

[48] B. Benlarbi, P. S. J. Russell, and L. Solymar, "Bragg diffraction of finite beams by thick gratings: two rival theories," Appl. Phys. B, Photophys. Laser Chem. **B28**, 63–72 (1982).

[49] R. K. Kostuk, J. W. Goodman, and L. Hesselink, "Volume reflection holograms with multiple gratings: an experimental and theoretical evaluation," Applied Optics **25**, 4362–4369 (1986).

Appendix A

Insights Provided by the Eigenvector Solution to the Coupled Wave Equations

The basic solution to the coupled-wave equations describing wave interactions in a single volume Bragg grating is straightforward but provides little insight into physical properties of the system. This is especially true when multiplexed volume holograms are considered and the system of differential equations grows much larger.

To illustrate some insights that can be gleaned from exploring the eigenvectors and eigenvalues of the system of coupled-wave equations as suggested in Section 2.1, the following sections look at these entities in two limits of the dephasing parameter, ϑ, viz. the Bragg-matched case where $\vartheta \to 0$ and the case of extreme Bragg mismatch where ϑ grows large.

A.1 Limit as $\vartheta \to 0$

Bragg-matching the input with the grating is equivalent mathematically to letting ϑ go to zero. In this situation, the eigenvalues of $\tilde{\boldsymbol{M}}$ become

$$\gamma_{\pm} = \pm j\sqrt{\frac{\kappa^2}{c_R c_S}}, \tag{A.1}$$

and the (normalized) eigenvectors representing the normal modes of the grating can be shown to be

$$\boldsymbol{\xi}_{\pm} = \frac{\sqrt{2}}{2}\begin{bmatrix} 1 \\ \pm 1 \end{bmatrix}. \tag{A.2}$$

Eigenvectors in this form imply that an input comprised of only the R wave (i.e. $\boldsymbol{x}_0 = \begin{bmatrix} 1 & 0 \end{bmatrix}^T$) will excite both eigenmodes of the grating—note that $\boldsymbol{x}_0 = \left(\boldsymbol{\xi}_+ + \boldsymbol{\xi}_-\right)/\sqrt{2}$, leading to energy transfer between the R and S waves. This is shown mathematically as

$$\begin{aligned} \boldsymbol{x}_d = \frac{1}{2} &\begin{bmatrix} \frac{1}{c_R} & 0 \\ 0 & \frac{1}{\sqrt{c_R c_S}} \end{bmatrix}\begin{bmatrix} 1 & 1 \\ 1 & -1 \end{bmatrix}\begin{bmatrix} e^{j\frac{\kappa d}{\sqrt{c_R c_S}}} & 0 \\ 0 & e^{-j\frac{\kappa d}{\sqrt{c_R c_S}}} \end{bmatrix} \\ &\times \begin{bmatrix} 1 & 1 \\ 1 & -1 \end{bmatrix}\begin{bmatrix} c_R & 0 \\ 0 & \sqrt{c_R c_S} \end{bmatrix}\begin{bmatrix} 1 \\ 0 \end{bmatrix} \\ = &\begin{bmatrix} \cos\left(\frac{\kappa d}{\sqrt{c_R c_S}}\right) \\ j\sqrt{\frac{c_R}{c_S}}\sin\left(\frac{\kappa d}{\sqrt{c_R c_S}}\right) \end{bmatrix}. \end{aligned} \tag{A.3}$$

Using Kogelnik's definition, the diffraction efficiency related to the S portion

of $\boldsymbol{x}_d$ is

$$\eta = \frac{c_S}{c_R} S_d S_d^* = \sin^2\left(\frac{\kappa d}{\sqrt{c_R c_S}}\right) \tag{A.4}$$

which is exactly 100% when the parameters of the grating are set such that $\kappa d/\sqrt{c_R c_S} = m\pi/2$ with m an odd integer. Equation A.4 matches Koglenik's result for a single lossless transmission grating.

Finally, note that when ϑ is not exactly 0, R_d and S_d will not be pure cosine and sine functions respectively, and they hence will not differ in phase by exactly $\pi/2$. Recall that ϑ is termed the *dephasing* parameter, and note that when the reference wave is not Bragg-matched with the grating (i.e. $\vartheta \neq 0$), at no point in z will one of R and S be a maximum while the other is a minimum. Hence, unless the reconstruction wave satisfies the Bragg condition, 100% diffraction efficiency is impossible.

A.2 Limit of $\vartheta \gg 2\sqrt{\frac{c_S}{c_R}\kappa}$

In the case where the the input wave is not Bragg-matched with the grating, we examine the system for $\vartheta \gg 2\sqrt{\frac{c_S}{c_R}\kappa}$. Here, the eigenvalues of $\tilde{\boldsymbol{M}}$ are

$$\gamma_+ = \frac{j\vartheta}{c_S} \tag{A.5a}$$

$$\gamma_- = 0, \tag{A.5b}$$

and the eigenvectors can be shown to be

$$\boldsymbol{\xi}_+ = \begin{bmatrix} 1 \\ 0 \end{bmatrix} \tag{A.6a}$$

$$\boldsymbol{\xi}_- = \begin{bmatrix} 0 \\ 1 \end{bmatrix}. \tag{A.6b}$$

In this case, an input comprised of only the R wave (i.e. $\boldsymbol{x}_0 = \begin{bmatrix} 1 & 0 \end{bmatrix}^T$) is, in fact, an eigenmode of the grating, and the only effect of the grating on this input will be a phase change. The second eigenmode (i.e. the S wave) will not be excited, and there will be no energy transfer between the R and S waves. This corresponds to a diffraction efficiency of 0.

Appendix B

Extending the Model to Support Reflection Gratings

Throughout the mathematical derivation of Chapter 2, the focus was on transmission gratings. However, the method introduced in that chapter is equally applicable to holographic elements consisting multiplexed reflection gratings and, in fact, elements consisting of both transmission and reflection gratings. (A similar mathematical formulation handling three multiplexed reflection gratings was previously reported [49]. The solution to the system involved a fourth-order Runge-Kutta algorithm for numerical integration.) To properly handle reflection gratings in an HOE, the boundary conditions used in the final stage of the matrix calculation must be revisited.

We discussed in Section 2.1 that the boundary conditions for solving the differential equations describing a single transmission grating were simply that $R(0)$, the amplitude of the input wave at $z = 0$, takes on some initial amplitude (e.g.

$R(0) = 1$), and $S(0)$, the amplitude of the output wave at $z = 0$, is exactly zero. For multiple transmission gratings in the holographic element, the boundary condition for the S_i waves in general is $S_i(0) = 0$ for all i. However, if one of the S_i waves describes the output of a reflection grating (i.e. the z-component of the corresponding $\boldsymbol{\sigma}_i$ vector is negative), this boundary condition is inappropriate. In this case, the amplitude of the wave at $z = d$ must be 0, and the wave amplitude at $z = 0$ is unknown and determined through the diffraction efficiency calculations.

The matrix equation for solving the system of equations describing the holographic element (see Eq. 2.23) is given as:

$$\boldsymbol{x}_d = \boldsymbol{G}\boldsymbol{x}_0 \tag{B.1}$$

If we assume that the S_i elements are sorted such that the associated plane waves are traveling in the $+z$ direction for $i \leq P$ and in the $-z$ direction for $P < i \leq N$, then we can write the boundary conditions for Eq. B.1 as:

$$\boldsymbol{x}_0 = \begin{bmatrix} R_0 \\ 0 \\ \vdots \\ 0 \\ s_{0(P+1)} \\ \vdots \\ s_{0N} \end{bmatrix} \tag{B.2}$$

and

$$\boldsymbol{x}_d = \begin{bmatrix} r_d \\ s_{d1} \\ \vdots \\ s_{dP} \\ 0 \\ \vdots \\ 0 \end{bmatrix} \tag{B.3}$$

where R_0 is known and r_d and all s_{0i} and s_{di} are unknown.

We can solve Eq. B.1 for these boundary conditions in two steps by taking advantage of the 0 entries in the $\boldsymbol{x}_0$ and $\boldsymbol{x}_d$ vectors. First, the 1st through Pth entries are removed from $\boldsymbol{x}_0$ and $\boldsymbol{x}_d$ producing $\boldsymbol{y}_0$ and $\boldsymbol{y}_d$ respectively.

$$\boldsymbol{y}_0 = \begin{bmatrix} R_0 \\ s_{0(P+1)} \\ \vdots \\ s_{0N} \end{bmatrix} \tag{B.4}$$

and

$$\boldsymbol{y}_d = \begin{bmatrix} r_d \\ 0 \\ \vdots \\ 0 \end{bmatrix} \tag{B.5}$$

Likewise, the 1st through Pth rows and columns are removed from $\boldsymbol{G}$ to produce

$\boldsymbol{H}$. This results in obtains the matrix equation:

$$\boldsymbol{y}_d = \boldsymbol{H}\boldsymbol{y}_0 \tag{B.6}$$

which represents a subset of the scalar equations underlying Eq. B.1.

Equation B.6 can be solved for $\boldsymbol{y}_0$ by inverting $\boldsymbol{H}$ and inserting any temporary value for r_d (e.g. 1). After rescaling $\boldsymbol{y}_0$ to obtain the appropriate value of R_0 and reinserting appropriate zero entries, $\boldsymbol{x}_0$ is recovered. This, in turn, can be inserted into Eq. B.1 to determine $\boldsymbol{x}_d$ thereby determining all unknowns.